Korean J. Chem. Eng., 40(4), 824-840 (2023)
DOI: 10.1007/s11814-022-1187-z

pISSN: 0256-1115
eISSN: 1975-7220

Carbon nanosheets coated on zirconium oxide nanoplate nanocomposite for Zn^{2+} ion adsorption and reuse of spent adsorbent for fingerprint detection

Bienvenu Gael Fouda-Mbanga, Eswaran Prabakaran, and Kriveshini Pillay†

Department of Chemical Sciences, University of Johannesburg, Doornfontein Campus, Johannesburg 2028, South Africa
(*Received 15 January 2022 • Revised 29 April 2022 • Accepted 23 May 2022*)

Abstract−This work highlights a novel method for the synthesis of carbon nanosheets coated on zirconium oxide nanoplate (CNS/ZrO_2NPs) nanocomposite that is used as an adsorbent for Zn^{2+} ions removal from water. CNS/ZrO_2NPs nanocomposite was prepared using CNS and ZrO_2NPs by a hydrothermal method. This nanocomposite proved to be a good adsorbent for Zn^{2+} ion uptake at maximum pH of 8 and dosage of 20 mg. The Temkin isotherm model represented the adsorption process followed by the Langmuir isotherm with a maximum adsorption capacity of 606.06 mg g^{-1}, above other adsorbents that have been reported for the removal of zinc ions. The adsorption kinetic process was best described by the pseudo-second-order kinetics, and it was found that the adsorption followed a chemisorption process. The thermodynamic parameters, such as enthalpy (ΔH), Gibbs free energy (ΔG), and entropy (ΔS), revealed that the adsorption was exothermic, spontaneous, and not random during the process. This metal-loaded adsorbent Zn^{2+}-CNS/ZrO_2NPs nanocomposite furthermore was reused in latent fingerprint detection and did demonstrate good selectivity and sensitivity on different surfaces by two donors. Therefore, Zn^{2+}-CNS/ZrO_2NPs nanocomposite may be reutilized as a good fingerprint marking agent in latent fingerprint (LFP) identification to circumvent secondary environmental pollution by the release of a spent adsorbent.

Keywords: Zinc, CNS/ZrO_2NPs Nanocomposite, Adsorption, Reuse, Latent Fingerprint (LFP)

INTRODUCTION

One of the greatest environmental challenges is the ecological emissions from heavy metals introduced by different anthropogenic activities, such as mining, energy and fuel manufacturing, electrical sports, wastewater sludge handling, and agriculture [1]. This is undoubtedly due to increasing industrialization, growing population, and total environmental health indifference. In general, heavy metals are found in soil and water components. However, due to anthropogenic activities, the prevalence of heavy metals in the environment has increasesd and groundwater systems have been poisoned worldwide [1]. Heavy metals are carried from the industrial site through runoff water and contaminated sources of water downstream. Before disposal, removal of these hazardous heavy metals from wastewater is necessary to prevent health hazards. Most of the heavy metals released into the wastewater are found to be harmful and carcinogenic and pose a significant threat to human health [2]. Among these toxic heavy metals is Zn^{2+}.

Zinc commonly exists in water systems. Industrial wastewaters contain zinc arising from corrosion, plating, galvanization and roller coating operations. Compounds made of zinc are used for various purposes, for example, $ZnCl_2$ is used for parchment production; ZnO is applied as a catalyst and $ZnSO_4$ is used as a fertilizer. Compounds of Zinc are present in pesticides and fungicides which eventually end up in water [3]. Exposure to zinc can lead to damage of the pancreas and lungs and can cause fever, appetite, hair loss, and decrease immunity. The recommended zinc concentration in the human body is 5 mg/L according to the food and drugs administration (FDA) [4,5].

Different techniques can be used to extract and separate heavy metals like ion exchange, precipitation, membrane filtration, adsorption, and electrochemistry from water and wastewater. The safest, simplest and cost-saving approach is adsorption since it is popularly utilized during the treatment processes for effluent [6]. In addition, cost-effective approaches such as safe agro-waste materials have emerged because they are environmentally friendly, cheaper, and easy to operate, unlike chemical methods.

Corn husks are byproducts in the maize industry. Countries, such as the United States of America, Eastern Europe, India and South Africa are big producers of maize (Zea mays L) worldwide. While maize is produced at numerous levels globally, it is primarily utilized for vegetable production, degradable polymers, biofuels, livestock feeding, and corn husk is used for paper production [7]. Furthermore, corn husk's structure is made up of cellulose, hemicellulose, lignin, and protein with hydroxyl, amid, and amine groups on its surface, making it selective and favorable to use as an adsorbent [7,8].

Lately, consideration has been shifted to metal oxide (MO) adsorbents such as Fe_2O_3 [9], Al_2O_3 [10], TiO_2 [11], MnO [12], ZrO_2 [13], CeO_2 [14], ZnO [15] and CuO [15]. These metal oxide nanoparticles were demonstrated to be good adsorbents for hazardous metal removal from water because of their expanded surface area and great activity created by size quantization [16]. Zirconia dioxide nanoparticles (ZrO_2NPs) are unreactive ceramic materials having

†To whom correspondence should be addressed.
E-mail: kriveshinip@uj.ac.za
Copyright by The Korean Institute of Chemical Engineers.

a broad range of uses because of their unique mixture of mechanical and physicochemical properties like excellent disintegration resistance, little conduction of heat, insulating properties, and excellent strength [17,18]. They are operated in thermal barrier coatings in jet turbines and diesel engines to operate at greater temperatures [19]. However, ZrO_2NPs have demonstrated critical disadvantages such as agglomeration, a low partition, intensive pressure decrease, flow system, low surface area, and less adsorption ability [20]. Hence, the modification of ZrO_2NPs is needed to increase the surface area and adsorption capacity for the removal of Zn^{2+} ions from wastewater samples.

Chitosan-ZrO_2 [21], Aliginate-ZrO_2 [22], Lignin-ZrO_2, Go-ZrO_2 [23], CNT-ZrO_2, Cdots-ZrO_2, Activated Carbon-ZrO_2, Mesoporous Carbon and carbon from agricultural waste have been used for zinc removal. Agricultural waste of carbon materials is easily available and is reused for economic development. Therefore, carbon modified ZrO_2NPs nanocomposite has been significantly implemented in the remediation of heavy metals because of their interesting properties such as preventing the metal oxide nanoparticle deprivation in the composite matrix. Furthermore, these nanocomposites have demonstrated larger surface areas, which is more favorable for adsorption [24].

In the past ten years, intensive studies have been conducted to remove heavy metals from water systems and to fight environmental pollution. However, the fate of metal-impregnated nanocomposites remains a challenge [25]. To tackle this issue, a few re-use applications including brick preparation, bio-energy, steel industry mainly in coal blend and coke oven. biologically mainly living microbes, photocatalysis and latent fingerprint detection (LFP) have been conducted to minimize secondary environmental pollution by disposal of the spent adsorbents [26,27].

There are three major kinds of fingerprint proofs that might be found in a crime scene. One of these is the beveled (or reshaped) fingerprint that seems to be a 3-dimensional fingermark in a tensile material like putty or candle wax. The second category is the noticeable fingermark that could be favorable or unfavorable depending on whether the fingers have been tarnished with a colored substance, like blood, or if the dust and soot have been cleared from the outside using the fingerprint ridges. Latent fingerprint detection is the most frequent form of fingerprint-proof and the one that causes the most concern. Latent fingerprint detection has shown to be a better tool for successful fingerprint identification at a crime scene [27]. A variety of chemical substances have been used to develop latent fingerprints onto substrates, including iodine fuming, ninhydrin, cyanoacrylate fuming, micro-particles, nanoparticles, fluorescence nanomaterials, rare earth upconverters fluorescent materials, polymer dots, aggregation-induced luminogens, conjugated polyelectrolyte, and heavy metals doped nanomaterials [28,29].

These markings are mostly undetectable, and usually need some sort of physiochemical handling to distinguish them from the substrate [30]. The physical development of the powder dusting method (PDM) has been the most practical and broadly applied technique for recovering and visualizing latent fingerprints because it is easy to operate for the user. However, all powders are not generally effective with daylight due to less background interference, less sensitivity, and low resolution images. Metal ion-loaded adsorbent powder has proved to be a good labeling agent for LFP detection on various non-porous and porous substrates due to electrostatic and hydrophobic interactions between the powder and ridge patterns [28].

In this article, the focus is on the synthesis of carbon nanosheets (CNS) derived from agricultural waste corn husk and modified with zirconium dioxide nanoparticle (ZrO_2NPs) nanocomposite. This has been applied as an adsorbent to remove Zn^{2+} ions from aqueous solutions and re-use the metal loaded adsorbent (Zn^{2+}-CNS/ZrO_2NPs nanocomposite) powder for LFP detection on various substrates to combat secondary pollution.

EXPERIMENTAL PROCEDURE

1. Materials

Corn husk waste was obtained from a local market in Johannesburg, South Africa. 98% Cadmium nitrate tetrahydrate, 98% Nickel nitrate hexahydrate, 99% Copper(II) nitrate trihydrate, and 98% Manganese chloride tetrahydrate, 99% Zinc nitrate hexahydrate, zirconium oxychloride were acquired from Sigma-Aldrich. 99% Lead nitrate, potassium bromide, sodium hydroxide, hydrochloric acid, and ethanol were obtained from Merck South Africa. Deionized water was applied for the stock solution preparation.

2. Synthesis of CNS from Corn Husk Powder

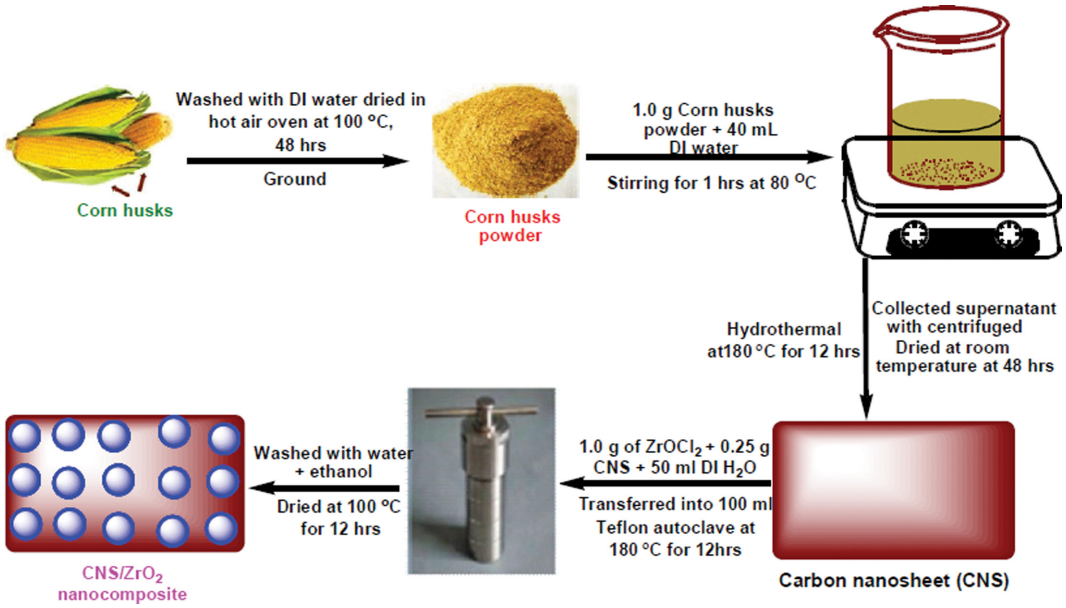
Corn husks were cut into pieces followed by washing with distilled water and later exposed to air for drying. In addition, the air-dried corn husks were introduced in a hot air oven at a hundred degrees Celsius for two days for further drying. The dried corn husks were pulverized to yield the powder and kept in 100 ml plastic bottles until appropriate analysis. A mixture of 40 ml of deionized water and 1.0 g of husk powder was heated at 80 degrees Celsius for one hour then transferred into an autoclave at 180 degrees Celsius for 12 hrs. After the thermal reaction was completed, the collected supernatant was centrifuged at 7,000 rpm for 30 min. Furthermore, the obtained solution was filtered to remove solid residues and left to air dry. After a few days, a dark brown CNS powder was collected and kept in plastic bottles.

3. Preparation of CNS/ZrO_2NPs Nanocomposite

CNS/ZrO_2NPs nanocomposite was prepared by mixing 1.0 g of ZrO_2NPs with 0.25 g CNS in 50 ml deionized water, which was adjusted at pH 7 then stirred for 24 h and transferred into 100 ml Teflon autoclave at 180 °C for 12 h. The mixture was centrifuged at 7,000 rpm for 30 min and then cleansed with water and ethanol a couple of times to eradicate any contamination. After centrifuging, the residue was gathered and placed into a hot air oven for drying purposes at 100 °C for 12 h. Scheme 1 illustrates the synthesis of the nanocomposite described above.

4. Characterization Techniques

FTIR spectrum of CNS, CNS/ZrO_2NPs nanocomposite was investigated using a Bruker Vertex 70 (Perkin Elmer, USA) by the KBr pellet method to determine the functional groups. A mechanical shaker was applied to shake the solutions. UV-VIS spectrophotometer was applied to find the absorption wavelength of the CNS/ZrO_2NPs nanocomposite. Malvern Nano zeta sizer 90 was operated to establish the stoutness and surface charge of the prepared CNS/ZrO_2NPs nanocomposite. This was achieved using the solu-



Scheme 1. Schematic diagram of CNS/ZrO_2NPs nanocomposite synthesis.

tion-state with 40 mg of CNS/ZrO_2NPs nanocomposite in 15 ml distilled water under the sonication for 30 minutes before analysis. ICP-OES was utilized to evaluate Zn^{2+} ions molarity after adsorption (Thermo Scientific, China) and 0.5 ml min^{-1} pumping speed. The pH tests were performed by an OHAUS to regulate the pH of the solution. Latent fingerprint (LFP) images were procured with a phone camera under normal visible light.

5. Adsorption Studies

Zn^{2+} ions solutions were made using appropriate dilutions from the concentrated solutions. The uptake analysis was achieved in triplicate with 20 mL of 50 mg L^{-1} Zn^{2+} ions mixture at pH 8.0± 0.2 and 20 mg of the nanocomposite, followed by agitating using a thermostatic water bath shaker at 200 rpm for 60 min. The influence of pH was evaluated by diversifying the starting pH (3-9) utilizing 50 mg L^{-1} of Zn^{2+} ions solution (prepared from deionized water and zinc nitrate hexahydrate). The regulation of pH was carried out by making use of both 0.1 molar hydrochloric acid and sodium hydroxide solution.

The amount of zinc adsorbed onto CNS/ZrO_2NPs nanocomposite was evaluated by taking advantage of Eqs. (1) and (2) as illustrated below.

$$q_e = \frac{(C_o - C_e)V}{m} \quad (1)$$

In which qe indicates the adsorption capacity, V the solution volume, m the weight of CNS/ZrO_2NPs nanocomposite in grams, Co and Ce being the starting and equilibrium molarity of Zn^{2+}.

$$\text{Removal efficiency}\,(\%) = \frac{(C_o - C_e)100}{C_o} \quad (2)$$

Uptake isotherms were examined at pH 8.0±0.2 at temperatures of 25, 30, and 35 °C with starting Zn^{2+} ion molarity in the span of 50-350 mg L^{-1} and 20 mg adsorbent dosage. In addition, the data obtained from isotherm studies were utilized to calculate the thermodynamic parameters including Gibbs free energy (ΔG^o), enthalpy (ΔH^o), and entropy (ΔS^o) change. Kinetics is important for the projection of the rate and modeling of water handling systems. This was investigated utilizing 20 mL solutions of various starting Zn^{2+} ions concentrations of 50-350 mg L^{-1} at 25 °C, 20 mg adsorbent dosage, and pH 8.0±0.2 for 0 to 60 minutes agitating. The capacity to adsorb q_t of the adsorbent was achieved by making use of Eq. (3):

$$q_t = \frac{(C_o - C_t)}{m} v \quad (3)$$

where q_t is the maximum equilibrium at time t and C_t the molarity of Zn^{2+} ions at time t.

The adsorption process with increasing temperatures may be described by applying the changes in standard thermodynamics parameters like Gibbs free energy, enthalpy, and entropy. The parameters of thermodynamics were determined using Eqs. (4) and (5) as seen below:

$$\ln k = \frac{\Delta S^o}{R} - \frac{\Delta H^o}{RT} \quad (4)$$

$$\Delta G^o = -RT\ln k \quad (5)$$

In which R and T are as described earlier, the equilibrium constant k is calculated from the CNS/ZrO_2NPs nanocomposite adsorbate proportion (q_e) to that of the solution in equilibrium (C_e).

6. Influence of Competing Ions

It was critical to explore the impact of ions competing for the ring adsorption process since no sole ion can be observed in the ordinary water system. Hence it is necessary to examine the impact of available bivalent ions on the binding site of CNS/ZrO_2NPs nanocomposite with the method described above. This was done by dispersing precursor salts of different ions Pb^{2+}, Cu^{2+}, Cd^{2+}, Mn^{2+}, and Ni^{2+} with Zn^{2+} ions at 50, 60, 70, 80, 90, and 100 mg L^{-1} molarity in de-ionized water. The obtained mixture was shaken by

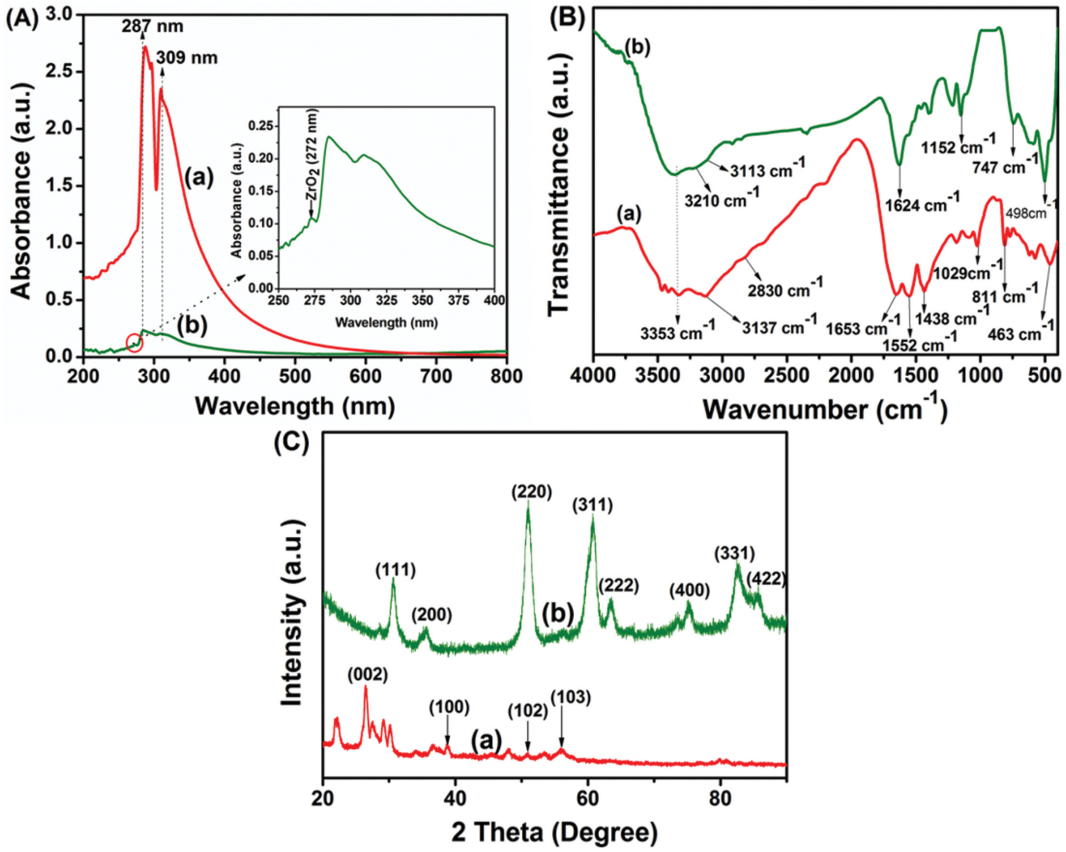


Fig. 1. (A) UV-visible spectra of (a) CNS and (b) CNS/ZrO_2NPs nanocomposite; (B) FTIR spectra of (a) CNS and (b) CNS/ZrO_2NPs nanocomposite; (C) XRD spectra of (a) CNS and (b) CNS/ZrO_2NPs nanocomposite.

making use of the optimized adsorbent dosage at pH 8.0±0.2 for 60 min, then analysis for the residual Zn^{2+} was carried out.

7. LFP Detection with Zn^{2+}-CNS/ZrO_2NPs Adsorbent by Physical Method

LFP identification was explored using PDM with reused cadmium bonded with adsorbent of Zn^{2+}-CNS/ZrO_2NPs identifying powder. Donors of fingerprints had their hands wiped and dried first. The fingers were then placed smoothly on the foreheads and nose, and the thumb impression was then implemented on distinguished substrates. Afterwards, the labeling powder of Zn^{2+}-CNS/ZrO_2NPs spread on the fingerprint and the excessive marking powder was wiped with a squirrel brush. A good phone with a high-resolution camera was utilized to capture the fingerprint images under daylight conditions.

8. Data Validation

Solution tests were obtained in triplicate for the metal ion concentration calculation in both studies. All graphs and tables show mean values±SD (error bars). The standard deviation from the mean was determined using Eq. (6) below:

$$SD = \sqrt{\frac{\sum_{i=1}^{n}(x_i - \bar{x})^2}{n-1}} \quad (6)$$

where n is the number of data points from the trial; x_i being the value of exclusive data point; x being the average data points

RESULTS AND DISCUSSION

1. Characterization

1-1. UV-Visible Study

Fig. 1(A)((a) & (b)) displays the UV-Vis spectra of CNS and CNS/ZrO_2NPs nanocomposite in an aqueous solution state. Fig. 1(A)(a) demonstrates that CNS exhibited two peaks at 284 and 307 nm which corresponded to n-π^* (C=O) and π-π^* (C=C) [32, 33]. The occurrence of these peaks confirmed the presence of carboxylic acid (COOH) and carbon groups on the CNS. Fig. 1(A)(b) shows that the CNS/ZrO_2NP nanocomposite spectra three peaks at 286, 312, and 272 nm, respectively. The lower intensity peaks observed at 286 and 312 nm showed a transfer of CNS coated on ZrO_2NPs wavelength shifted peaks when compared to the pure CNS [45]. Additionally, a low-intensity peak was observed at 272 nm and demonstrated the presence of Zr-O bond in ZrO_2NPs as shown in Fig. 1(A)(b) (inset) [32]. These peaks successfully demonstrated the formation of CNS/ZrO_2NPs nanocomposite.

1-2. FTIR Analysis

Fourier transform infrared spectroscopy was conducted to ascertain the functional groups present on CNS and CNS/ZrO_2NPs nanocomposite as shown in Fig. 1(B)((a) & (b)). CNS spectra peaks at 3,355, 2,976, 1,684, 1,458, 1,223, and 1,059 cm^{-1} corresponded, respectively, to the extending vibration and bending of OH, C-H, COOH, C=C, C-OH, $=CH_2$ as displayed in Fig. 1(B)(a) [34,35].

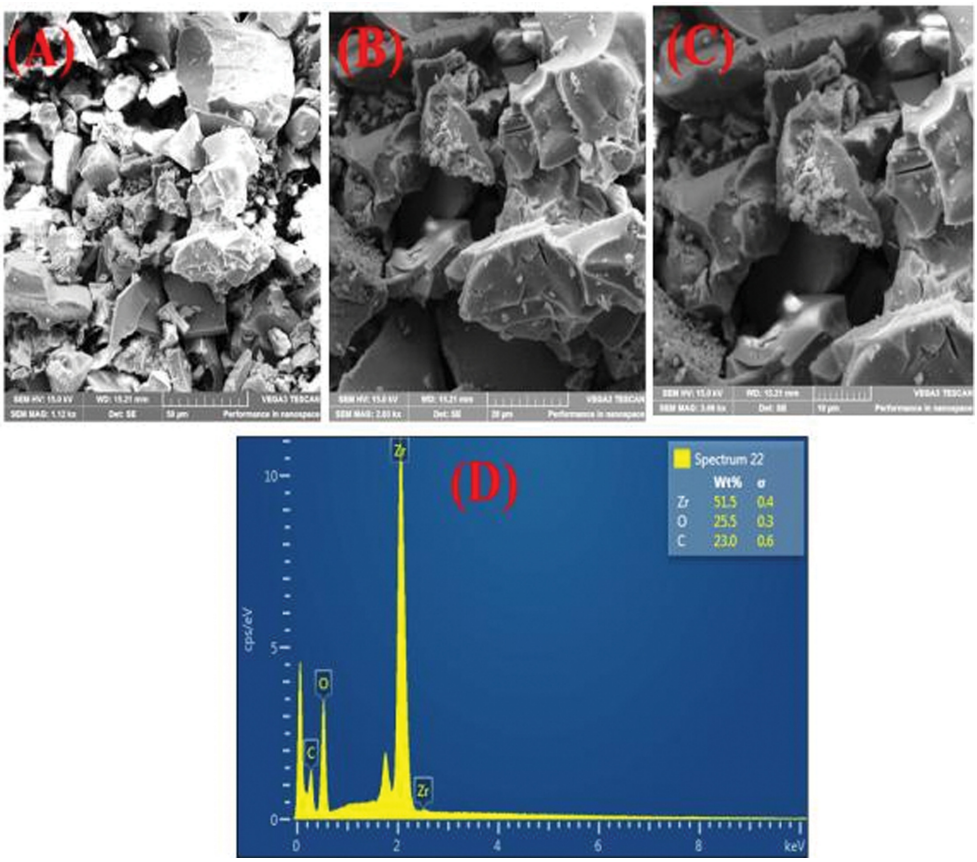


Fig. 2. SEM images of CNS/ZrO_2NPs nanocomposite at various magnifications of (A) 50 μm, (B) 20 μm, (C) 10 μm and (D) EDAX.

The above-mentioned peaks confirmed the successful formation of CNS. Fig. 1(B)(b) shows the CNS/ZrO_2NPs nanocomposite spectrum in which the peak intensity decreased and also slightly shifted the peak position after ZrO_2NPs were coated on the CNS nanocomposite [36]. Additionally, the apexes observed at 699 and 618 cm^{-1} corresponded to m-ZrO_2 and ZrO_3^{-2} group vibrational modes, which supported the presence of ZrO_2 [34]. The above confirmed the attachment of CNS on ZrO_2NPs forming the CNS/ZrO_2NPs nanocomposite.

1-3. XRD Spectra

Fig. 1(C) shows the XRD diffraction pattern of CNS and CNS/ZrO_2NPs nanocomposite, respectively. Fig. 1(C)(a) exhibits four peaks which diffracted at 26.60°, 38.68°, 51.16°, 56.05° corresponding to (002), (100), (102), (103) crystal planes. The first three peaks demonstrate the sp^2 nature and the last peak shows the sp^3 carbon-like structure [35]. CNS/ZrO_2NPs nanocomposite yielded several diffraction patterns observed at 26.05°, 28.25°, 33.08°, 39.21°, 48.64°, 53.70°, 58.31°, 61.15° which corresponded to (111), (200), (220), (311), (222), (400), (331) and (422) as shown in Fig. 1(C)(b). These diffraction pattern peaks matched the monoclinic configuration based on the International Center for Diffraction Data (ICDD) 37-1484 [36]. Furthermore, the reduction in intensity observed in CNS/ZrO_2NPs nanocomposite revealed CNS was coated on ZrO_2NPs. The average crystalline size of CNS (21.97 nm) and CNS/ZrO_2NPs nanocomposite (5.50 nm) was determined using Scherrer's formula with respective peaks at 28.91° (002) and 48.64° (022).

1-4. Surface Morphology Analysis

Fig. 2(A)-(C) shows CNS/ZrO_2NPs nanocomposite images acquired at distinctive magnifications of 50 μm, 20 μm, and 10 μm. A mixture of CNS and ZrO_2NPs was observed as shown in Fig. 2(A). At higher magnification of 20 μm and 10 μm, a white deposit of ZrO_2NPs on CNS was observed, which confirmed the formation of CNS/ZrO_2NPs nanocomposite as illustrated in Fig. 2(B)-(C). Fig. 2(D) shows the EDX spectrum of CNS/ZrO_2NPs nanocomposite with peaks of C, O, and Zr, which further confirms the formation of the nanocomposite.

1-5. TEM Characterization

CNS/ZrO_2NPs nanocomposite TEM images at a specific magnification of 200, 100, and 50 nm are depicted in Fig. 3. At a lower magnification of 200 nm there was an aggregation of CNS with ZrO_2NPs as seen in Fig. 3(A), dispersion of the nanomaterials with thin plate-like-shapes was observed at higher magnification of 100 and 50 nm as illustrated in Fig. 3(B) & (C). Furthermore, there was the clustering of CNS with ZrO_2NPs while some have been isolated demonstrated the presence of electrostatic forces [37]. The selected area electron diffraction (SAED) as shown in Fig. 3(D) exhibited visible diffraction rings, which indicated the crystalline nature of ZrO_2NPs. Additionally, the presence of white particles of ZrO_2NPs was clearly embedded in CNS forming the composite [37].

1-6. X-Ray Photoelectron (XPS) Investigation

The composition surface of CNS/ZrO_2NPs nanocomposite and

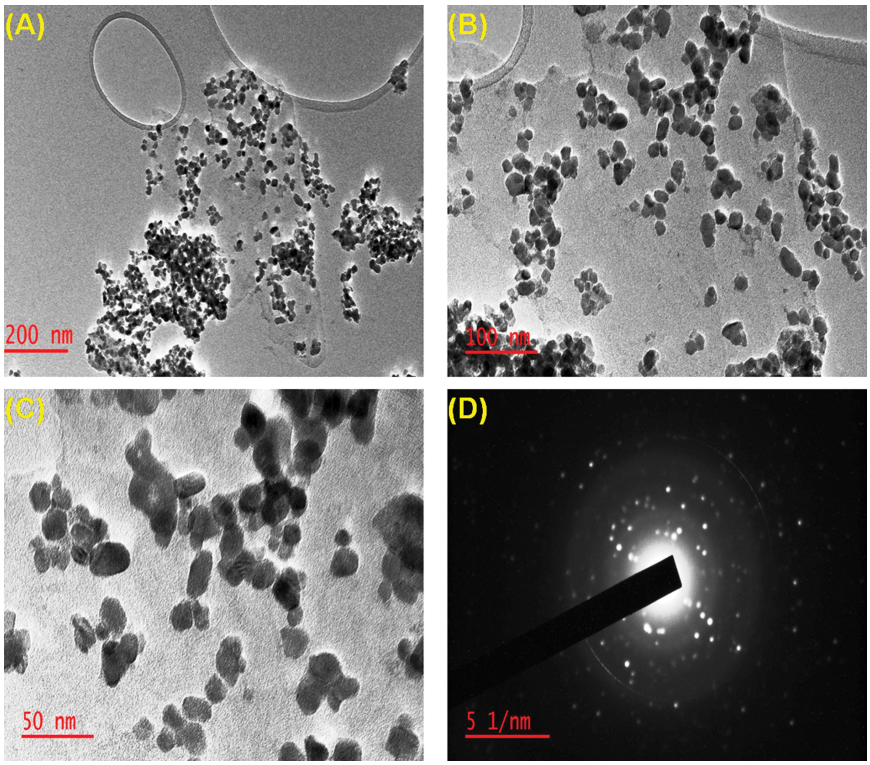


Fig. 3. TEM images of CNS/ZrO_2NPs nanocomposite at different magnifications of (A) 200 nm, (B) 100 nm, (C) 50 nm, and (D) SAED.

its electronic structures were established using XPS [38]. Fig. 4(a) illustrates the CNS/ZrO_2NPs nanocomposite XPS spectra, which indicate the presence of C, O, and Zr. The energy bands at 27.99, 51.94, 183.83, 283.67, 331.57, 427.37, 527.22, 974.49, 1,226.13 eV correlated independently with the critical levels of Zr 4p, Zr 4s, Zr 3d, C 1s, Zr 3p, Zr 3s, O KLL, C KLL [39]. Fig. 4(b) depicts the deconvolution of the essential level spectrum of C 1s with four peaks corresponding to C-C, Zr-C, C=O, and O-C=O at 283.67, 286.06, 286.38, 287.74 eV, respectively [42-44]. The core-level spectrum deconvolution of the O 1s provided three peaks at 531.82, 534.71, 537.12, and 538.75 eV, corresponding individually to the bonding of Zr^{4+}-O, Zr-OH, C-OH, C-O as illustrated in Fig. 4(c) [43]. The essential level-spectrum of Zr 3d reveals the presence of Zr $3d_{5/2}$ and Zr $3d_{3/2}$ spin-orbit doublet peaks at 179.13 and 181.30 eV, respectively, as seen in Fig. 4(d). The deconvolution of Zr 3d further demonstrates the presence of three types of species, mainly Zr^0, Zr^{4+}, Zr^{2+} corresponding to the binding energy at 178.39, 178.96, and 179.53 eV, respectively. The binding energy at 182.89 eV corresponded to Zr-O [44]. Fig. 4(e) displays the peaks of Zr $3p_{3/2}$ and Zr $3p_{5/2}$ with the binding energy of 329.89 and 343.47 eV.

2. Adsorption Studies

2-1. pH Influence on the Zn^{2+} Adsorption

The pH of a solution is a significant factor that influences the process of adsorption. The effect on the removal of Zn^{2+} ions from pH 3 to 10 was evaluated by using 0.01 g of CNS/ZrO_2NPs nanocomposite in a solution of 50 mg L^{-1} Zn^{2+} ions in 20 mL as represented in Fig. 5(a). The adsorption happened from pH 5 to 8 with a percentage removal of 0-99.12%. The maximum sorption is observed at pH 8. Thereafter, it remains constant until pH 10. At pH below the pH_{PZC} (4.94), Zn^{2+} ions interact in the acidic range on CNS/ZrO_2NPs nanocomposite with H^+ ions for active adsorption sites, resulting in electrostatic repulsion between the positive surface charge of CNS/ZrO_2NPs nanocomposite and Zn^{2+}. Hence insignificant adsorption was observed. At pH above pH_{PZC} (4.94), the remarkable adsorption of Zn^{2+} on CNS/ZrO_2NPs nanocomposite was due to the electrostatic connection of the negative surface of CNS/ZrO_2NPs nanocomposite and Zn^{2+} [26].

2-2. Dosage Influence on Zn^{2+} Adsorption

The influence of CNS/ZrO_2NPs nanocomposite dosage on Zn^{2+} intake from aqueous solution using 50 mg L^{-1} was investigated by diversifying the CNS/ZrO_2NPs nanocomposite mass from 10 mg to 60 mg at pH 8 for 60 min, as demonstrated in Fig. 5(b). The removal percentage of Zn^{2+} increased with increasing adsorbent dose from 10 to 20 mg and then dropped quickly to 40 mg due to more masses on the existing site of CNS/ZrO_2NPs nanocomposite, which was not exploited in smaller concentrations of Zn^{2+} ion solution. It was noticed that CNS/ZrO_2NPs nanocomposite had the highest percentage removal of Zn(II) at 27.20 percent at 20 mg as seen in Fig. 5(b). Furthermore, a slight increase of Zn^{2+} uptake was noted as the dosage was increased from 40 to 50 mg, then afterward a considerable decline of Zn^{2+} followed as represented in Fig. 5(b). The significant decline in efficiency at higher CNS/ZrO_2NPs nanocomposite dosage may be interpreted in terms of adsorbent partial aggregation, resulting in a decrease in the effective surface area for metal absorption [45].

2-3. Zeta Potential Analysis

The Zeta potential of CNS/ZrO_2NPs nanocomposite was explored at different pH, mainly 2 to 10, as displayed in Fig. 5(c). The sur-

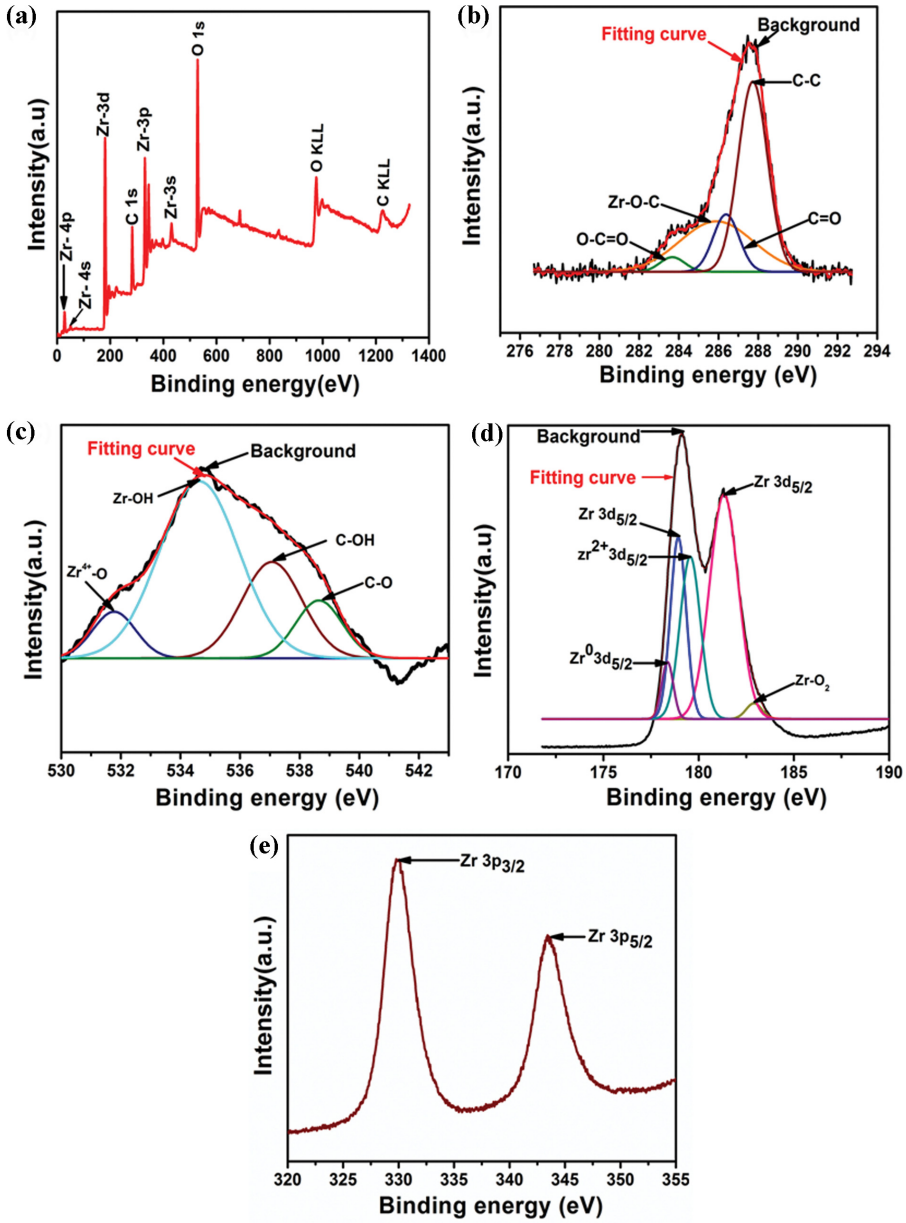


Fig. 4. XPS spectra of CNS/ZrO_2NPs nanocomposite of (a) Survey spectrum and Fitting curve of (b) C 1s, (c) O 1s and (d) Zr 3d, and (e) Zr 3p.

face charge of CNS/ZrO_2NPs nanocomposite appears to become positive at lower pH, which is caused by the protonation of hydroxyl groups on the nanocomposite under acidic conditions [46]. At higher pH, the surface charge of CNS/ZrO_2NPs nanocomposite becomes negatively charged due to the deprotonation of hydroxyl groups of the CNS/ZrO_2NPs nanocomposite, yielding more formation of hydroxyl groups on the zirconia surface (ZrO_2-OH) [47]. The point of zero charge of CNS/ZrO_2NPs nanocomposite was 4.94, as shown in Fig. 5(c). Hence, this data demonstrates the negative charge of CNS/ZrO_2NPs nanocomposite adsorbent above pH_{PZC} and depicts a good ability to adsorb Zn^{2+} ions from aqueous solution.

2-4. Adsorption Isotherms Studies

Adsorption capacity of an adsorbent and the relation between the ion and the adsorbent can be explained by isotherms. The characteristics of the uptake were assessed by describing Langmuir, Freundlich, Temkin, and D-R isotherms. Langmuir isotherm analysis investigated the efficiency of absorption of CNS/ZrO_2NPs nanocomposite using the Langmuir Eqs. (7) and (8) illustrated below:

$$\frac{C_e}{q_e}=\frac{C_e}{q_e}+\frac{1}{bq_m} \tag{7}$$

Eq. (1) might be rearranged as:

$$\frac{1}{q_e}=\frac{1}{bq_mC_e}+\frac{1}{q_m} \tag{8}$$

In which C_e in mg L^{-1} is the equilibrium concentration, q_e in mg g^{-1} is the equilibrium uptake amount, q_m is the highest uptake amount, and b is the Langmuir constant which is associated with

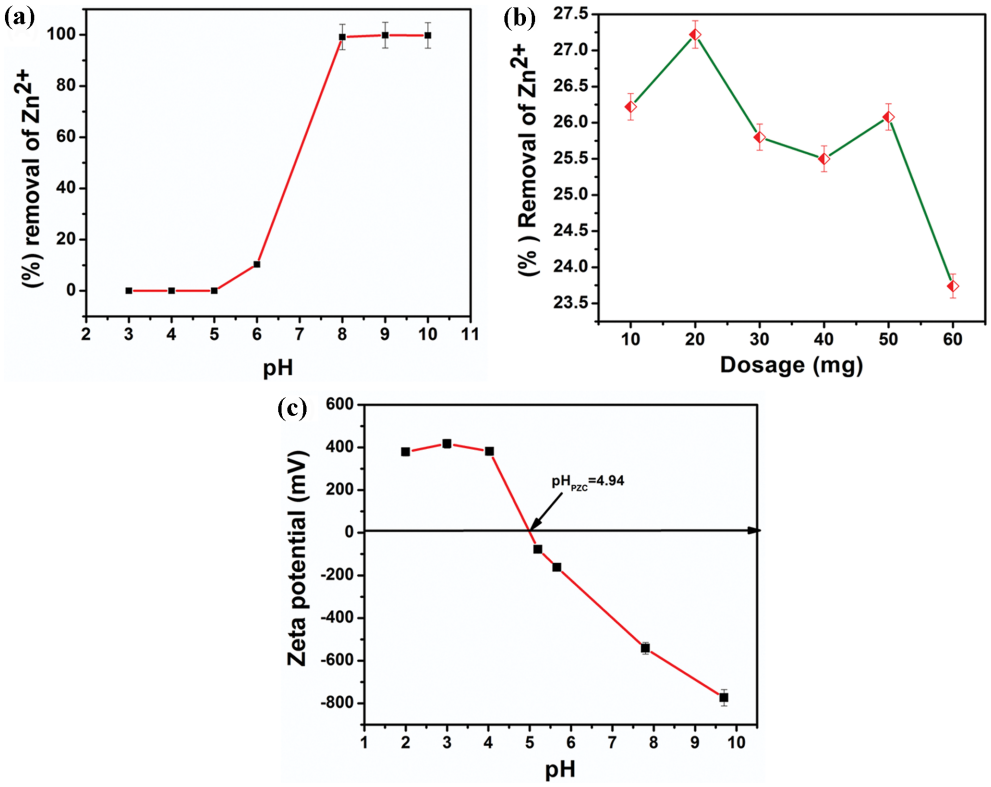


Fig. 5. (a) Effect of pH varying from 3 to 10, (b) effect of dosage, at 25 °C, 200 rpm, (c) Determination of point of zero charge of CNS/ZrO_2NPs nanocomposite with different pH 2 to 10.

Table 1. Isotherm model of Zn^{2+} ions adsorption capacity of CNS/ZrO_2NPs nanocomposite at different temperatures

Model	Temperature (°C)			
	25	35	45	55
Langmuir				
q_m (mg g^{-1})	606.06±0.05	333.33±0.048	194.93±0.034	258.40±0.062
K_L (L mg^{-1})	0.52	0.92	0.072	32.10
R_L	(5.46-37.07)×10^{-3}	(2.12-21.28)×10^{-3}	(38.17-217.39)×10^{-3}	(0.89-6.23)×10^{-4}
R^2	0.9999	0.938	0.857	0.649
Freundlich				
K_f(mg g^{-1})	161.69±0.025	266.99±0.036	18.29±0.059	333.37±0.074
1/n	0.515	2.029	0.575	0.323
R^2	0.816	0.910	0.832	0.652
Temkin				
K_t (L g^{-1})	10.65	12.37	1.002	52.74
b	82.69	100.78	57.28	88.56
R^2	0.973	0.856	0.973	0.719
D-R				
q (mg g^{-1})	301.21±0.053	324.55±0.036	223.50±0.063	329.49±0.035
$K_{D\text{-}R}$ (mol^2/kJ^2)×10^{-8}	4.269	6.888	6455.42	1.11
R^2	0.976	0.856	0.641	0.736
No. of points Evaluated	6	6	6	6

adsorption capacity and adsorption energy. For the Langmuir, Isotherm $1/q_e$ is plotted against $1/C_e$ as shown in Fig. 6(c). The maximum capacity to adsorb Zn^{2+} ion was 606.06 mg g^{-1} at 25 °C, as shown in Table 1. To assess if adsorption was appropriate, the non-

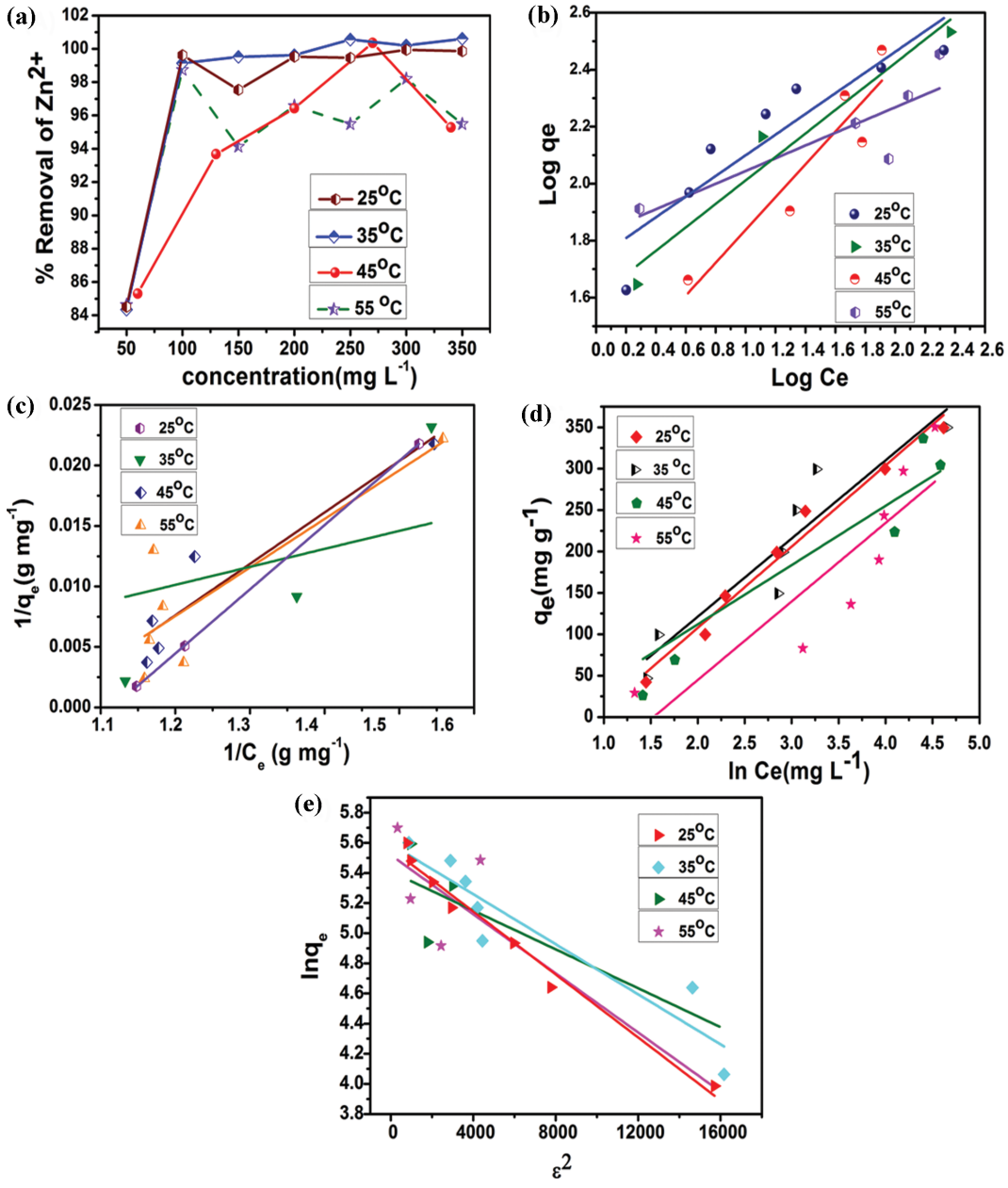


Fig. 6. (a) The maximum adsorption capacity of Zn^{2+} adsorbed on CNS/ZrO_2NPs nanocomposite, (b) Freundlich linear model, (c) Langmuir linear model, (d) Temkin linear model, and (e) D-R linear model of Zn^{2+} ions at 60 min, 200 rpm at different temperature.

dimensional factor R_L was taken into account and could be estimated as expressed in Eq. (9):

$$R_L = \frac{1}{1+K_L C_o} \tag{9}$$

The estimated value of the separation factor R_L at various initial concentrations in the range of 0.000089-0.22 is demonstrated in Table 1. The initial concentration of Zn^{2+} ions is given by C_0 and K_L is the Langmuir constant. When R_L is less than 1, then adsorption is advantageous; when R_L is higher than unity, then adsorption is not advantageous, and R_L being 0 is irreversible. Hence, the uptake in this study was favorable due to the value of R_L that was below 1 [48].

The Freundlich isotherm, as represented in Fig. 6(b), has defined the multilayer adsorption isotherm of CNS/ZrO_2NPs nanocomposite in which the equation that defines it is represented by Eq. (10):

$$\log q_e = \log K_f + \frac{1}{n}\log C_e \tag{10}$$

where K_f is the Freundlich constant describing the uptake capacity and n adsorption intensity. The rate of adsorption intensity n may be applied as: n equal to 1 represents a linear uptake; when n is less than 1, there is a chemical process; and if n is greater than 1, the uptake is a physical process. However, this can be regarded as if 1/n values close to zero imply further homogeneity of the surface. The values of n in the range of 1 to 10, on the other hand,

reveal strong adsorption [49]. The values of K_f and 1/n are presented in Table 1 and suggest favorable adsorption.

Temkin isotherm, as illustrated in Fig. 6(d), was applied to describe the adsorbent CNS/ZrO_2NPs nanocomposite and Zn^{2+} uptake interactions that differ with adsorbent surface coverage based on the free adsorption capacity. In addition, as a result of increased surface coverage, the adsorption heat of all molecules in the substrate is assumed to decrease linearly.

Temkin isotherm linear form was represented with Eq. (11) shown below:

$$q_e = B\ln k_T + B\ln C_e \tag{11}$$

where B is the Temkin isotherm constant obtained from the slope and k_T from the intercept (kJ/mol). Temkin parameters are shown in Table 1.

The Dubinin-Radushkevich (D-R) isotherm model has been implemented to explain the data of adsorption as represented in Fig. 6(e). It enhances the uptake process and provides as well as the mean free energy through the adsorption approach. The linear form of the D-R isotherm is given in Eq. (12) where $\ln q_e$ is plotted against ε^2:

$$\ln q_e = \ln q_s - \beta\varepsilon^2 \tag{12}$$

$$\varepsilon = RT\ln\left(1+\frac{1}{C_e}\right) \tag{13}$$

From Eqs. (12) and (13), R is the gas constant, T is the temperature in kelvin, q_s is the D-R theoretical saturation capacity and ε is the Polanyi potential, β is the activity coefficient linked to the uptake energy [50]. D-R parameters are depicted in Table 1. The mean free energy, E (kJ mol^{-1}) is determined from β and is represented as illustrated in Eq. (14):

$$E = \frac{1}{\sqrt{2\beta}} \tag{14}$$

This amount E is helpful because it gives insight regarding the adsorption process mechanisms. When E is between 8 and 16 kJ mol^{-1}, the adsorption process is chemical; however, if E<8 kJ mol^{-1}, the process is physical. In this work, the mean uptake energy was between 0.088-6.71 kJ/mol, which suggests that the procedure may be occurring physically. Based on the above four isotherm models, it could be concluded that the Temkin isotherm well describes the process since it demonstrates the highest average value of R^2 followed by the Langmuir model.

Figs. S5-S7 display the experimental outcomes that were done with the aid of different amounts of Zn^{2+} ions for Langmuir, Freundlich and Temkin non-linear isotherm models, and their respective Eqs. (15)-(17) are shown below. These were supported to establish a relation between equilibrium concentration and adsorption capacity. These adsorption models separately predicted the accuracy of adsorption activity.

Langmuir

$$q_e = \frac{q_m K C_e}{1+K C_e} \tag{15}$$

Freundlich isotherm model

$$q = K_F (C_e)^{1/n} \tag{16}$$

Temkin isotherm model

$$q = B\ln(K_T C_e) \tag{17}$$

Freundlich, Langmuir and Temkin isotherm parameters are shown in Table S1 Comparing the results obtained from the linear and the nonlinear models, it was observed that linear modeling was more appropriate in this investigation than the non-linear modeling.

The optimum adsorption capacity determined in this study was contrasted with other reported adsorbents as shown in Table 2.

Fig. 6(a) describes the percentage removal of Zn^{2+} adsorbed onto CNS/ZrO_2NPs nanocomposite against varying temperature concentrations. The percentage removal of Zn^{2+} has been observed to increase with the rise of concentration, as demonstrated in Fig. 6(a). After reaching maximum, Zn^{2+} ions (99.60%) have been removed at about 98.54 mg L^{-1}, a constant plateau was observed.

2-5. Adsorption Kinetic Studies

The uptake of Zn^{2+} ions at different temperatures against a period of contact time was investigated as depicted in Fig. 7(a). Gener-

Table 2. Comparative evaluation of Zn^{2+} ions adsorption capacity of CNS/ZrO_2NPs nanocomposite with other reported materials

Adsorbent	Adsorption capacity (mg g^{-1})	pH range	Reference
$MnFe_2O_4$	454.5	6	[51]
$CoFe_2O_4$	384.6	6	[51]
Tricalcium aluminate	892.45	6-7	[52]
NAg_2O-$NTiO_2$	127.6	6-7	[53]
GO	246	7	[54]
Maghemite nanotube	86.95	6	[55]
Fe_3O_4-MnO_2 nanoplate	100.24	6.49	[56]
Birnessite electrode	530.0	5.5	[57]
MOCS	0.116	6	[58]
Fe_3O_4-SiO_2	119	6	[59]
CNPs/ZrO_2	606.06	8	Current work

$MnFe_2O_4$: Manganese ferrite nanoparticles, $CoFe_2O_4$: Cobalt ferrite nanoparticles, Fe_3O_4-MnO_2: Magnetite-Manganese oxide nanocomposites, Fe_3O_4-SiO_2: Magnetite-silica nanocomposites, GO: Graphene oxide, MOCS: Manganese oxide-coated sand, NAg_2O-$NTiO_2$: nano titanium oxide-coated-silver oxide

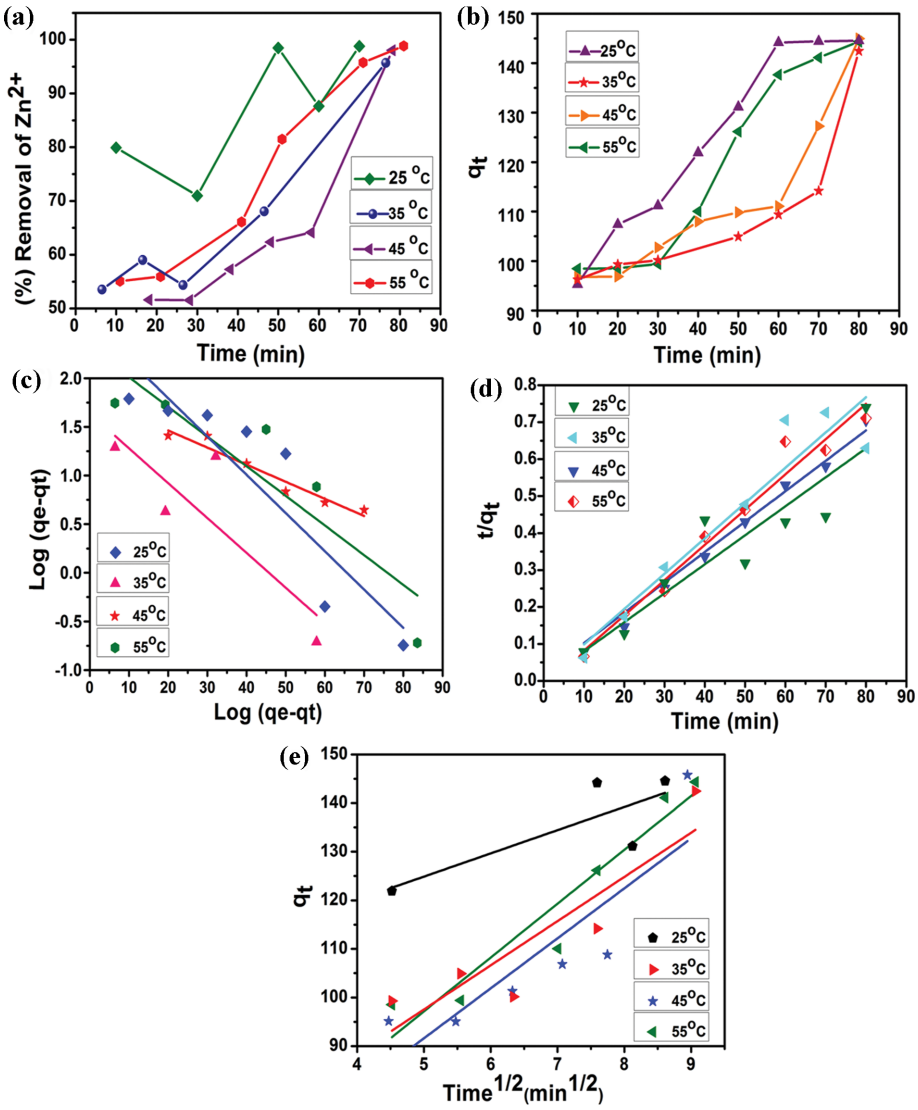


Fig. 7. (a) The percentage removal of Zn^{2+} by CNS/ZrO_2NPs nanocomposite (b) maximum adsorption capacity of Zn^{2+} adsorbed on CNS/ZrO_2NPs nanocomposite at equilibrium time, (c) pseudo-first-order kinetic model and (d) Pseudo-second-order kinetic model, (e) Intraparticle diffusion model.

ally, the initial adsorption rapidly inicreases under the temperature condition because of the greater concentration gradient between the adsorbate and the uptake site of the adsorbent surface. Upon reaching equilibrium the uptake rate will decrease [60]. Adsorption kinetics is crucial as it gives an understanding of the design and modeling of adsorption based on the water handling approach. Furthermore, the adsorbent must possess fast adsorption kinetics to be regarded for an eventual practical application [61]. Fig. 7(b) shows the maximum adsorption capacity of Zn^{2+} adsorbed on CNS/ZrO_2NPs nanocomposite at equilibrium time. To describe well the adsorption of Zn^{2+} onto CNS/ZrO_2NPs nanocomposite, kinetics that is pseudo-first-order, pseudo-second-order, and intra-particle diffusion were investigated using Eqs. (18), (19), (20), respectively, as shown below:

$$\log(q_e - q_t) = \log q_e - \frac{k_1}{2.303}t \tag{18}$$

$$\frac{t}{q_t} = \frac{1}{k_2 q_e^2} + \frac{t}{q_e} \tag{19}$$

$$q_t = k_{int}t^{1/2} + C_i \tag{20}$$

In which q_e and q_t are the uptake capacity at equilibrium and time t of metal ions adsorbed in mg g^{-1}; k_1 and k_2 are the rates constant in g mg^{-1}·min^{-1}; k_{int} mg g^{-1} $min^{-1/2}$ and C_i mg g^{-1} are the intra-particle diffusion rate constant and constant related to the magnitude of the boundary layer thickness, respectively.

The linear plot fittings Fig. 7(c)-(e) from which the various kinetic parameters were determined are displayed in Table 3. The R^2 of both pseudo-first-order and second-order exhibited in Table 3 were compared and pseudo-second-order kinetic values (0.820-0.997) were higher than pseudo-first-order values (0.521-0.921). Furthermore, the experimental and theoretical values of q_e correlated favorably with the pseudo-second-order rather than the pseudo-first-order

Table 3. Kinetics parameters for the adsorption of Zn^{2+} ions by CNS/ZrO_2NPs nanocomposite at different temperatures

Kinetic models	Temperature (°C)			
	25	35	45	55
Pseudo-first-order				
q_e (mg g^{-1})	382.51±0.04	48.76±0.054	43.59±0.027	29.04±0.048
k_1 (min^{-1})	0.091	0.0097	0.042	0.0081
R^2	0.790	0.591	0.759	0.929
No. of points evaluated	7	4	5	6
Pseudo-second-order				
q_e (mg g^{-1})	119.90±0.78	128.87±0.96	104.82±0.86	121.51±0.35
k_2 (g m^{-1} min^{-1})	0.043	0.0011	0.0025	0.0034
R^2	0.820	0.884	0.965	0.997
No. of points evaluated	8	7	8	8
Intraparticle diffusion constant				
k_{int} (mg/g·min)$^{1/2}$	4.69	7.15	3.26	3.63
C_i	105.86	70.57	58.22	71.79
R^2	0.464	0.744	0.694	0.899
No. of points evaluated	4	5	6	6

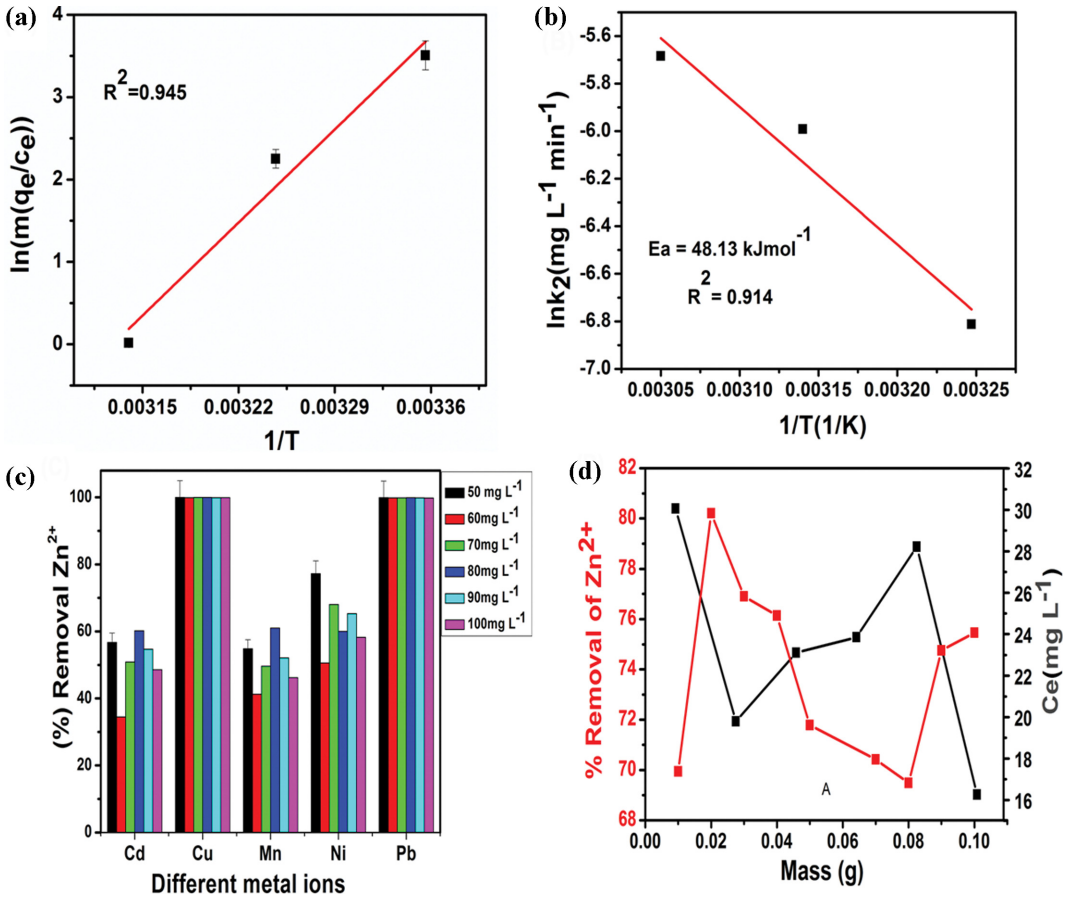


Fig. 8. (a) Adsorption thermodynamic, (b) Adsorption activation energy, (c) Effect of coexisting ions, and (d) Application on real water samples.

model. It was thus assumed that the uptake matched the kinetic model of the pseudo-second-order model. The rate is constant of the pseudo-second-order model increases at a high temperature, which indicates that the uptake of Zn^{2+} is strengthened at high temperature [60]. The intraparticle diffusion model as stated by Webber-Morris was evaluated to identify if a rate-limiting step existed or not. It is said that intraparticle diffusion governs the process if the graph qt vs $t^{1/2}$ becomes linear. In addition, intraparticle diffu-

Table 4. Thermodynamic Parameters for Zn^{2+} ions by CNP/ZrO_2NPs nanocomposite at 25 °C

Temperature	Metal ion	ΔH^o (kJ mol^{-1})	ΔS^o (J mol^{-1} K^{-1})	ΔG^o (kJ mol^{-1})	R^2
298 K	Zn^{2+}	−134.14	−419.65	−9.084	0.945
308 K	Zn^{2+}			−4.888	
318 K	Zn^{2+}			−0.691	
328 K	Zn^{2+}			3.505	

sion is verified to be the main step influencing uptake when the graph passes by zero. It may not be the unique rate-controlling step if it does not pass through zero. It can be shown that intraparticle diffusion was not the single rate control stage in Zn^{2+} adsorption onto CNS/ZrO_2NPs nanocomposite as the graph did not pass through zero as shown in Fig. 7(e) [62].

2-6. Determination of Activation Energy

To decide if the uptake mechanism was chemical or physical, the rate constant k_2 values from the pseudo-second-order kinetics were fitted against the reciprocal temperature values from the Arrhenius Eq. (21) as illustrated below [63]:

$$\ln k_2 = \ln A - \frac{E_a}{RT} \quad (21)$$

In which A is the frequency factor (g/mg·min), E_a is the energy of activation (kJ/mol), T is the temperature in Kelvin, R is the gas constant (8.314 kJ/mol·K).

Fig. 8(b) depicts the graph of $\ln k_2$ against 1/T where the activation energy is calculated as 48.13 kJ/mol which suggests chemical sorption between Zn^{2+} and CNS/ZrO_2NPs nanocomposite since the activation energy is above 40 kJ, as suggested by Velempini et al. [64].

2-7. Adsorption Thermodynamics for Zn^{2+} on CNS/ZrO_2NPs Nanocomposite

A graph of ln k_d against 1/T was plotted as shown in Fig. 8(a). The thermodynamics parameters are illustrated in Table 4. The negative value of Gibbs energy and enthalpy reveals that the uptake is spontaneous and exothermic, respectively. Furthermore, the enthalpy value of −134.14 kJ/mol<−80 kJ/mol implies that the process was chemisorption as demonstrated earlier by the activation energy. The negative value of the entropy indicates the non-randomness during adsorption [65].

3. Effect of Co-existing Ions

In both natural and wastewater, large numbers of ions are available at the same time. Fig. 8(c) demonstrates the influence of cations like Cd^{2+}, Cu^{2+}, Mn^{2+}, Ni^{2+}, Pb^{2+} on the intake of Zn^{2+} onto CNS/ZrO_2NP nanocomposite. Zn^{2+} adsorption was affected by Cd^{2+}, Mn^{2+}, Ni^{2+}, with a greater impact of Cd^{2+} on Zn^{2+} adsorption. The greater concentration of infused heavy metal ions led to significant interaction between heavy metal ions. The rise in the concentration of Cd^{2+} from 50 to 100 mg L^{-1} resulted in a reduction in Zn^{2+} adsorption from 60.31% to 34.54%, as depicted in Fig. 8(c). The interference order was Cd^{2+}>Mn^{2+}>Ni^{2+}>Cu^{2+}=Pb^{2+}. Furthermore, the order of the intervening ions may be centered on a charge per radius value (Z/R). The greater the value of charge to the radius, the greater the ion becomes attracted to the adsorbent's binding site.

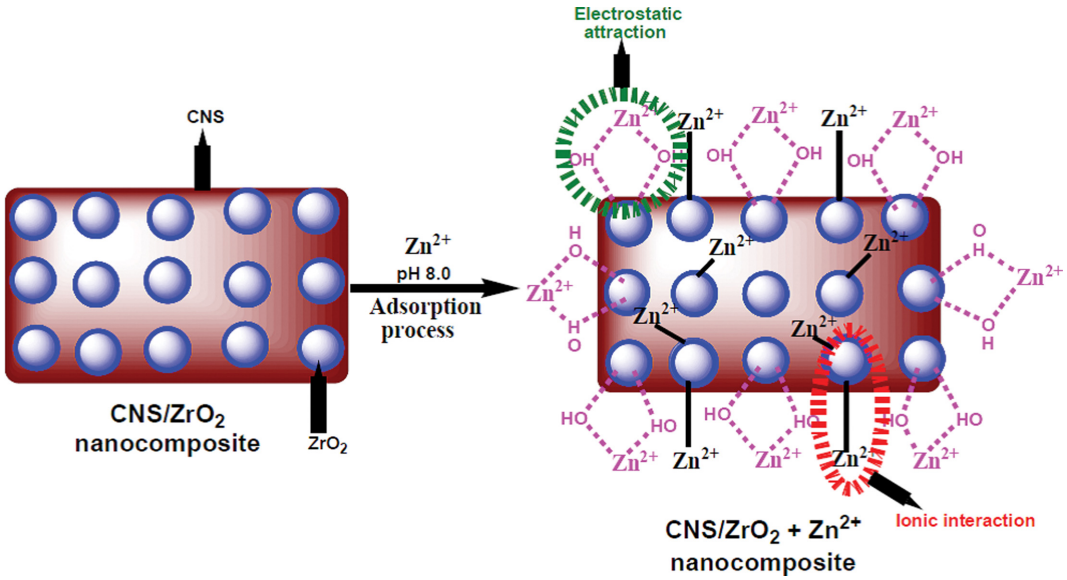
This interference order is strongly associated with cation Z/R values Cd^{2+}(2/0.95)>Mn^{2+}(2/0.70)>Ni^{2+}(2/0.70)>Cu^{2+}(2/0.73)>Pb^{2+}(2/1.19). Cu^{2+} and Pb^{2+} have less impact on the intake of Zn^{2+} due to repulsive forces owing to an electron affinity identical to zinc. Strong metal ion properties including ionic potential, electronegativity, hydroxylation softness, and position in the Irving-Williams series distinguished the adsorption amongst heavy metal ion adsorption [26].

4. Implementation of CNS/ZrO_2NPs Nanocomposite on Real Water Sample

To assess the effectiveness of Zn^{2+} extraction by CNS/ZrO_2NPs nanocomposite in industrial wastewater, a river stream water sample was located at the following geographical location of 26°16′28.7″S 28°02′53.5″E at Vorster Avenue, Glenanda, South of Johannesburg, South Africa, and the collected water sample was kept under cool conditions. The initial pH measured of this water sample was 6.89 with an initial Zn^{2+} concentration of 0.0498 mg L^{-1}. This was later brought to pH 8 and the concentration of Zn^{2+} spiked to 100 mg L^{-1}. Additionally, the prepared water sample was mixed with doses of CNS/ZrO_2NPs nanocomposite in the range of 0.01-0.1 g in a 20 ml sample solution. The mixture was then shaken for 60 min at 25 °C, 200 rpm. The percentage uptake and concentration at equilibrium of Zn^{2+} as the dosage increases is depicted in Fig. 8(d). In this graph, the percentage removal of Zn^{2+} increases from 69.94 to an optimum of 80.21% at 0.02 g; afterwards, a considerable decrease in zinc uptake follows until 69.98% at 0.08 g, then slightly increases again until 74.75%. Simultaneously, the equilibrium concentration of Zn^{2+} decreases with increasing dosage from 0.01 to 0.03 g with optimum equilibrium concentration at 30.52 mg L^{-1}, then it rapidly increases from 0.03 g to 0.08 g followed by another decrease until 0.1 g. CNS/ZrO_2NPs nanocomposite has therefore demonstrated the ability to reduce Zn^{2+} ions level in water from 100 to 16.26 mg L^{-1} value, which is above the allowable value of 5 mg L^{-1} as recommended by the Environmental Protective Agency (EPA) [66].

5. Adsorption Mechanism

The adsorption mechanism of Zn^{2+} onto CNS/ZrO_2NPs nanocomposite was carried out at pH 8; as discussed earlier, the surface charge of the nanocomposite becomes negatively charged due to dehydroxylation. The uptake could be influenced by the association of numerous mechanisms, such as complexation, ion exchange, and electrostatic interactions, which usually compete with one another [26]. To affirm this hypothesis, the FTIR spectrum of CNS/ZrO_2NPs nanocomposite, as shown earlier on in Fig. 1(B)(b), demonstrated the presence of numerous functional groups including -COOH, -OH that could interconnect with Zn^{2+} in different ways as seen in Scheme 2. The uptake of Zn^{2+} was achieved through electrostatic attraction between the negative surface of the adsorbent and the positively charged ions. Furthermore, Zn^{2+} adsorption was carried out through ionic interactions where H^+ is released



Scheme 2. Adsorption mechanism of Zn^{2+} ions using CNS/ZrO_2NPs nanocomposite.

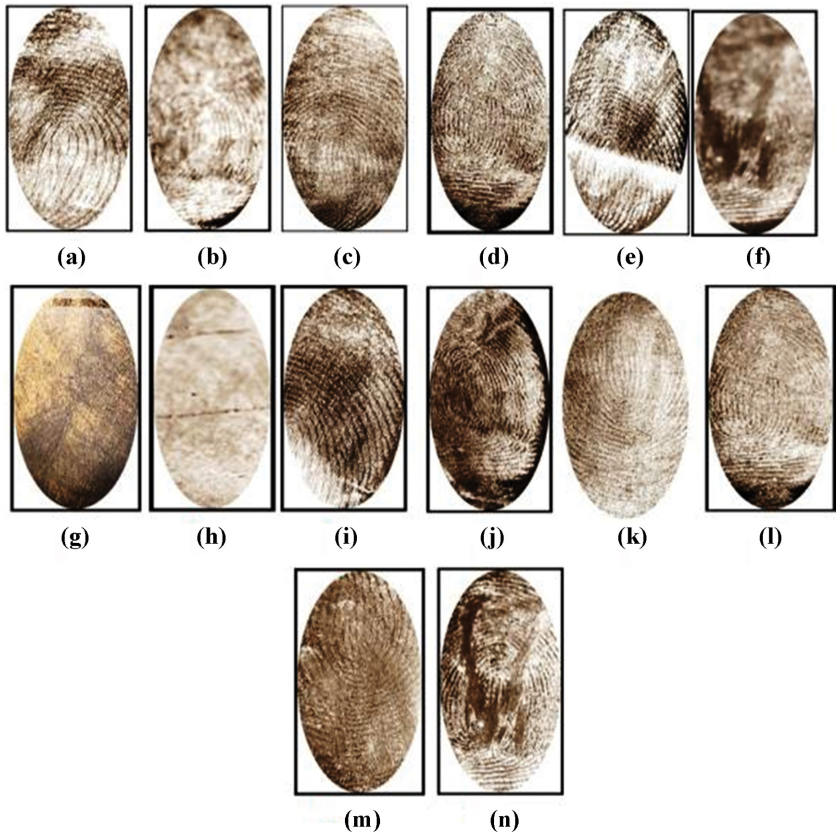


Fig. 9. (a)-(n) LFP images with CNS/ZrO_2NPs nanocomposite on aluminum foil (a) donor 1, (b) donor 2; aluminum sheet (c) donor 1, (d) donor 2, glass slide (e) donor 1, (f) donor 2; compact disc (g) donor 1, (h) donor 2; aluminum foil after 3 days (i) donor 1, (j) donor 2; aluminum sheet after 3 days (k) donor 1, (l) donor 2, glass slide after 3 days (m) donor 1, (n) donor 2.

during the process. The cation exchange reaction between H^+ and Zn^{2+} at the adsorbent surface site could involve the following steps:

$$(\text{-COOH})+Zn^{2+}+H_2O\rightarrow(\text{-COO})Zn^{+}+H_3O^{+} \quad (22)$$

$$2(\text{-COOH})+Zn^{2+}+2H_2O\rightarrow(\text{-COO})_2Zn+2H_3O^{+} \quad (23)$$

$$(\text{-C-OH})+Zn^{2+}+H_2O\rightarrow(\text{-C=O})Zn^{+}+H_3O^{+} \quad (24)$$

The above reactions (1-3) take place on the assumption that H^+ on

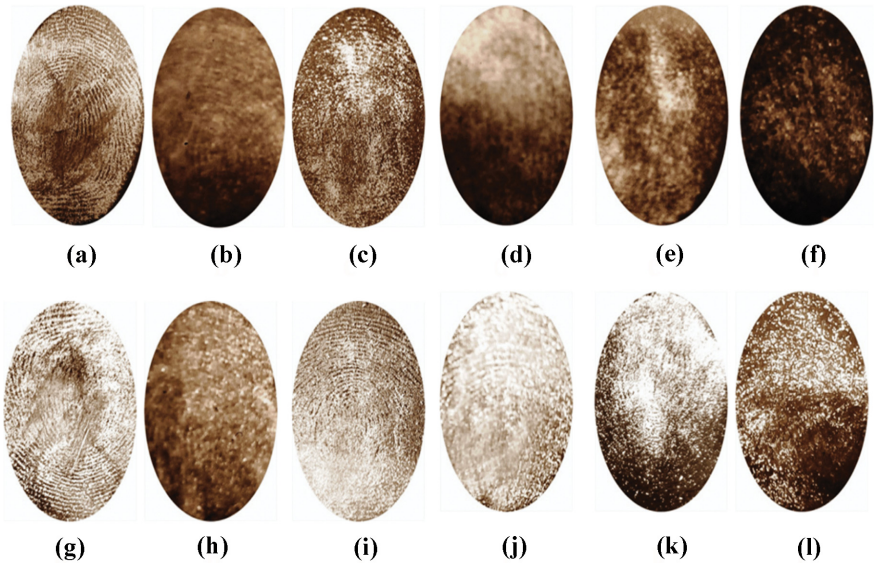


Fig. 10. (a)-(l) LFP images with Zn^{2+}-CNS/ZrO_2NPs nanocomposite on aluminum foil (a) donor 1, (b) donor 2; aluminum sheet (c) donor 1, (d) donor 2, glass slide (e) donor 1, (f) donor 2; aluminum sheet after 5 days (g) donor 1, (h) donor 2; aluminum foil after 5 days (i) donor 1, (j) donor 2, glass slide after 5 days (k) donor 1, (l) donor 2.

Table 5. Performance comparison of CNS/ZrO_2NPs nanocomposite for LFP detection with other reported materials

Material	Method	Substrates	LFP detection	References
N-CDs/ZnONPs	Hydrothermal	Aluminum foil	1, 2, 3	[70]
CDs/SiO_2	Pyrolysis	Glass slide	1, 2, 3	[71]
CDs@TiO_2	Hydrothermal	Aluminum foil	1, 2, 3	[72]
N-CDs	Microwave	Filter paper	1	[73]
CNMs	Solvothermal	Aluminum foil	1, 2	[74]
SNPs	Thermochemical	Glass slide	1	[75]
CNS/ZrO_2NPs nanocomposite	Hydrothermal	Aluminum sheet	1, 2	Own work

-C-OH and -COOH will be exchanged by Zn^{2+} since these functional groups are assumed to be responsible for Zn^{2+} adsorption [41,42].

6. Application of the Spent Adsorbent (Zn^{2+}-CNS/ZrO_2NPs Nanocomposite) in Latent Fingerprint Detection

The synthesized nanocomposite was demonstrated to be efficient in removing Zn^{2+} ions from water. The spent adsorbent was obtained after adsorption of Zn^{2+} on CNS/ZrO_2NPs nanocomposite, and the reuse of this spent adsorbent was investigated for LFP detection. The latent fingerprint (LFP) comparison of two separate donors was conducted on different non-porous surfaces like a glass rod, aluminum sheet, aluminum foil and compact disc using CNS/ZrO_2NPs nanocomposite and Zn^{2+}-CNS/ZrO_2NPs nanocomposite powder as a labeling agent under daylight as shown in Figs. 9 & 10. CNS/ZrO_2NPs nanocomposite gave better images with clear fingerprint patterns on aluminum foil using donor 2 rather than donor 1 as illustrated with daylight conditions in Fig. 9(a) & (b). Furthermore, LFP aging for three days was developed. It was observed that there was still visibility of LFP ridge patterns on all the substrates with aluminum foil yielding better images when applying using donor 2 as seen in Fig. 9(i) & (j). Usually, the fluorescence of a good labeling agent can last for up to four weeks [69]. LFP using Zn^{2+}-CNS/ZrO_2NPs nanocomposite as a labeling agent was investigated as well as demonstrated in Fig. 10(a)-(l). Better images with clear fingerprint patterns were obtained with donor 2 when applied on aluminum foil under daylight conditions as shown in Fig. 10(a). Additionally, visible and better patterns were obtained on aluminum foil after an interval period of five days, thus demonstrating the viability of Zn^{2+}-CNS/ZrO_2NPs nanocomposite as an identification agent in LFP as seen in Fig. 10(g). Table 5 illustrates the comparison of CNS/ZrO_2NPs nanocomposite LFP performance with other reported materials.

CONCLUSION

The removal of Zn^{2+} from water samples was successfully undertaken using CNS/ZrO_2NPs nanocomposite as adsorbent. The optimum dosage (20 mg) and pH 8 were obtained along with the highest percentage extraction of 99%, respectively. Several isotherm models were applied and CNS/ZrO_2NPs nanocomposite was best described by the Langmuir isotherm model for the removal of Zn^{2+} ions at pH 8 with the optimum adsorption capacity q_{max} value of 606.06 mg g^{-1} at 25 °C. The adsorption kinetics was best described by second-order kinetics, which was obtained by high cor-

relation coefficient R^2 and experimental adsorption capacity q_e. The thermodynamic parameters such as Gibbs energy and enthalpy demonstrated that the adsorption process was spontaneous and exothermic. The activation energy revealed that the process was chemisorption. The efficiency of CNS/ZrO_2NPs nanocomposite adsorbent was tested on real water samples for the removal of Zn^{2+} ions and it exhibited a good adsorption capacity at pH 8. Furthermore, a reuse study was implemented in this work through LFP identification where the metal-loaded adsorbent Zn^{2+}-CNS/ZrO_2NPs nanocomposite was applied as a marking agent by PDM under daylight. Zn^{2+}-CNS/ZrO_2NPs nanocomposite was applied on various substrates by two different donors to establish fingerprint identification, and it demonstrated to be a better prospective marking agent for LFP detection in crime investigations. Therefore, the adsorbent could be marketed for LFP detection once it has reached its utmost zinc loading capacity instead of disposing it into the environment.

ACKNOWLEDGEMENTS

The Chemical Sciences department, University of Johannesburg, South Africa, financially supported this work. The work was also supported by the NRF (National Research Foundation). A sincere thanks are extended to Profs Emanuela Carleschi and Bryan Doyle for conducting the XPS analysis.

AUTHOR CONTRIBUTIONS

Bienvenu Gael Fouda Mbanga for conceptualization, data procuration, Eswaran Prabakaran for visualization, Kriveshini Pillay for guidance and supervision have equally contributed.

Declaration

The authors declare no competing financial interest.

SUPPORTING INFORMATION

Additional information as noted in the text. This information is available via the Internet at http://www.springer.com/chemistry/journal/11814.

REFERENCES

1. F. A. Rejula and M. Dhinakaran, *Res. J. Recent Sci.*, **1**, 2 (2012).
2. D. Lakherwal, *IJERD*, **4**, 1 (2014).
3. K. Trivunac, Z. Sekulić and S. Stevanović, *J. Serb. Chem. Soc.*, **77**, 1661 (2012).
4. S. M. Kanawade and R. W. Gaikwad, *Int. J. Chem. Eng. Appl.*, **2**, 199 (2011).
5. V. Vaishnav, S. Chandra and K. Daga, *Int. J. Sci. Eng. Res.*, **2**, 12 (2011).
6. H. M. Zwain, M. Vakili and I. Dahlan, *Int. J. Chem. Eng.*, **2014** (2014).
7. Z. Tevassolirizi, K. Shams and M. R. Omidkhah, *J. Ind. Eng. Chem.*, **23** (2015).
8. S. Indah, D. Helard and A. Sasmita, *Water Sci. Technol.*, **73**, 12 (2016).
9. S. Dixit and J. G. Hering, *Environ. Sci. Technol.*, **37**, 4182 (2003).
10. A. K. Patra, A. Dutta and A. Bhaumik, *J. Hazard. Mater.*, **201**-**202**, 170 (2012).
11. Z. Xu, Q. Li, S. Gao and J. K. Shang, *Water Res.*, **44**, 5713 (2010).
12. B. J. Lafferty, M. Ginder-Vogel and D. L. Sparks, *Environ. Sci. Technol.*, **44**, 8460 (2010).
13. C. Hang, Q. Li, S. Gao and J. K. Shang, *Ind. Eng. Chem. Res.*, **51**, 353 (2012).
14. A. R. Contreras, E. Casals, V. Puntes, D. Komilis, A. Sánchez and X. Font, *Glob. Nest J.*, **17**, 536 (2015).
15. S. Mahdavi, M. Jalali and A. Afkhami, in Nanotechnol. Sustain. Dev. (2012).
16. R. Taman, O. Me and F. Ha, *J. Adv. Chem. Eng.*, **5**, 3 (2015).
17. D. L. Trejo-Arroyo, K. E. Acosta, J. C. Cruz, A. M. Valenzuela-Muñiz, R. E. Vega-Azamar and L. F. Jiménez, *Appl. Sci.*, **9**, 1 (2019).
18. C. V. Reddy, B. Babu, I. N. Reddy and J. Shim, *Ceram. Int.*, **44**, 6940 (2018).
19. M. Negahdary, A. Habibi-Tamijani, A. Asadi and S. Ayati, *J. Chem.*, **2013** (2012).
20. J. Yang, B. Hou, J. Wang, B. Tian, J. Bi, N. Wang, X. Li and X. Huang, *Nanomaterials*, **9**, 424 (2019).
21. M. Ahmad, S. Ahmed and S. Ikram, *Int. J. Pharmacogn.*, **2**, 280 (2015).
22. S. M. Prabhu and S. Meenakshi, *Carbohydr. Polym.*, **120**, 60 (2015).
23. E. Zong, D. Wei, H. Wan, S. Zheng, Z. Xu and D. Zhu, *Chem. Eng. J.*, **221**, 193 (2013).
24. T. A. Dontsova, S. V. Nahirniak and I. M. Astrelin, *J. Nanomater.*, **2019** (2019).
25. L. J. Johnston, N. Gonzalez-Rojano, K. J. Wilkinson and B. Xing, *NanoImpact*, **18**, 100219 (2020).
26. B. G. Fouda-Mbanga, E. Prabakaran and K. Pillay, *Arab. J. Chem.*, **13**, 6762 (2020).
27. C. Lennard, INTERPOL Forensic Science Symposium (2001).
28. O. P. Jasuja and G. Singh, *Forensic Sci. Int.*, **192**, e11 (2009).
29. A. Mukherjee, M. K. Adak, P. Dhak and D. Dhak, *J. Environ. Sci. (China)*, **88**, 301 (2020).
30. M. Wang, M. Li, A. Yu, Y. Zhu, M. Yang and C. Mao, *Adv. Funct. Mater.*, **27**, 14 (2017).
31. W. S. B. Dwandaru, A. L. Fadli, E. K. Sari and Isnaeni, *Dig. J. Nanomater. Biostructures*, **15**, 555 (2020).
32. M. J. Deka, P. Dutta, S. Sarma, O. K. Medhi, N. C. Talukdar and D. Chowdhury, *Heliyon*, **5**, e01985 (2019).
33. S. Vivekanandhan, M. Venkateswarlu, H. R. Rawls and N. Satyanarayana, *Mater. Chem. Phys.*, **120**, 148 (2010).
34. T. N. Rao, I. Hussain, J. E. Lee, A. Kumar and B. H. Koo, *Appl. Sci.*, **9**, 17 (2019).
35. L. A. Chunduri, A. Kurdekar, S. Patnaik, B. V. Dev, T. M. Rattan and V. Kamisetti, *Mater. Focus.*, **5**, 1 (2016).
36. E. De La Rosa-Cruz, L. A. Díaz-Torres, P. Salas, V. M. Castaño and J. M. Hernández, *J. Phys. D. Appl. Phys.*, **34**, 2 (2001).
37. F. H. Alhassan, U. Rashid and Y. H. Taufiq-Yap, *J. Oleo Sci.*, **64**, 505 (2015).
38. X. Yin, X. Xie, L. Song, Y. Zhou, P. Du and J. Xiong, *J. Mater. Sci.*, **52**, 11025 (2017).
39. L. Sygellou, V. Gianneta, N. Xanthopoulos, D. Skarlatos, S. Georga,

C. Krontiras, S. Ladas and S. Kennou, *Surf. Sci. Spectra*, **18**, 58 (2011).
40. H. Estrade-Szwarckopf, *Carbon N. Y.*, **42**, 1713 (2004).
41. H. Zhou, F. Z. Zhou, Y. Q. Shen, B. Liao, J. J. Yu and X. Zhang, *Chinese Phys. Lett.*, **35**, 066202 (2018).
42. Y. Liu and X. Jing, *Carbon N. Y.*, **45**, 1965 (2007).
43. S. R. Teeparthi, E. W. Awin and R. Kumar, *Sci. Rep.*, **8**, 1 (2018).
44. P. Lackner, Z. Zou, S. Mayr, U. Diebold and M. Schmid, *Phys. Chem. Chem. Phys.*, **21**, 17613 (2019).
45. S. A. Bhalerao, A. S. Sharma and S. D. Maind, *Int. J. Adv. Res. Biol. Sci.*, **2**, 136 (2015).
46. H. Keramati, M. H. Saidi and M. Zabetian, *J. Dispers. Sci. Technol.*, **37**, 6 (2016).
47. F. E. Bortot Coelho, V. M. Candelario, E. M. R. Araújo, T. L. S. Miranda and G. Magnacca, *Nanomaterials*, **10**, 779 (2020).
48. S. A. Chaudhry, T. A. Khan and I. Ali, *Egypt. J. Basic Appl. Sci.*, **3**, 287 (2016).
49. M. Karnib, A. Kabbani, H. Holail and Z. Olama, *Energy Procedia.*, **50** (2014).
50. S. Debnath, A. Maity and K. Pillay, *J. Environ. Chem. Eng.*, **2**, 260 (2014).
51. R. Asadi, H. Abdollahi, M. Gharabaghi and Z. Boroumand, *Adv. Powder Technol.*, **31**, 1480 (2020).
52. M. S. Mansour, M. E. Ossman and H. A. Farag, *Desalination*, **272**, 301 (2011).
53. T. Wang, P. Zhang, D. Wu, M. Sun, Y. Deng and R. L. Frost, *J. Colloid Interface Sci.*, **443**, 65 (2015).
54. M. E. Mahmoud, E. A. Saad, A. M. El-Khatib, M. A. Soliman and E. A. Allam, *Prog. Nucl. Energy*, **106**, 51 (2018).
55. H. Wang, X. Yuan, Y. Wu, H. Huang, G. Zeng, Y. Liu, X. Wang, N. Lin and Y. Qi, *Appl. Surf. Sci.*, **279**, 432 (2013).
56. M. H. Al-Malack and A. A. Basaleh, *Desalin. Water Treat.*, **57**, 24519 (2016).
57. A. Roy and J. Bhattacharya, *Chem. Eng. J.*, **211**-**212**, 493 (2012).
58. J. Zhao, J. Liu, N. Li, W. Wang, J. Nan, Z. Zhao and F. Cui, *Chem. Eng. J.*, **304**, 737 (2016).
59. L. Liu, Y. Luo, W. Tan, F. Liu, S.L. Suib, Y. Zhang and G. Qiu, *Environ. Sci. Nano*, **4**, 811 (2017).
60. T. Velempini, K. Pillay, X. Y. Mbianda and O. A. Arotiba, *J. Environ. Sci. (China)*, **79**, 280 (2019).
61. M. Chigondo, H. Kamdem Paumo, M. Bhaumik, K. Pillay and A. Maity, *J. Colloid Interface Sci.*, **532**, 500 (2018).
62. E. C. Umejuru, E. Prabakaran and K. Pillay, *Results Mater.*, **7**, 100117 (2020).
63. A. A. Jalil, S. Triwahyono, M. R. Yaakob, Z. Z. A. Azmi, N. Sapawe, N. H. N. Kamarudin, H. D. Setiabudi, N. F. Jaafar, S. M. Sidik, S. H. Adam and B. H. Hameed, *Bioresour. Technol.*, **120**, 218 (2012).
64. T. Velempini, K. Pillay, X. Y. Mbianda and O. A. Arotiba, *J. Environ. Sci. (China)*, **79**, 280 (2019).
65. K. Parashar, N. Ballav, S. Debnath, K. Pillay and A. Maity, *J. Colloid Interface Sci.*, **476**, 103 (2016).
66. M. Hassan, L. Begun, S. Hosain, P. Poddar, A. Chowdhury and F. Ali, *J. Environ. Anal. Toxicol.*, **7**, 433 (2017).
67. J. Wang and C. Chen, *Biotechnol. Adv.*, **27**, 195 (2009).
68. Y. Bulut and Z. Tez, *J. Environ. Sci.*, **19**, 160 (2007).
69. E. Prabakaran and K. Pillay, *J. Saudi Chem. Soc.*, **24**, 584 (2020).
70. E. Prabakaran and K. Pillay, *Arab. J. Chem.*, **13**, 3817 (2020).
71. L. Ma, Z. Xia, V. Atuchin, M. Molokeev, S. Auluck, A. H. Reshak and Q. Liu, *Phys. Chem. Chem. Phys.*, **17**, 31188 (2015).
72. F. Li, H. Li and T. Cui, *Opt. Mater. (Amst)*, **73**, 459 (2017).
73. Y. P. Sun, B. Zhou, Y. Lin, W. Wang, K. A. S. Fernando, P. Pathak, M. J. Meziani, B. A. Harruff, X. Wang, H. Wang, P. G. Luo, H. Yang, M. E. Kose, B. Chen, L. M. Veca and S. Y. Xie, *J. Am. Chem. Soc.*, **128**, 7756 (2006).
74. F. Li, X. Wang, W. Liu, L. Wang and G. Wang, *Opt. Mater. (Amst)*, **86**, 79 (2018).
75. R. Rajan, Y. Zakaria, S. Shamsuddin and N. F. Nik Hassan, *Egypt. J. Forensic Sci.*, **9**, 1 (2019).

Supporting Information

Carbon nanosheets coated on zirconium oxide nanoplate nanocomposite for Zn^{2+} ion adsorption and reuse of spent adsorbent for fingerprint detection

Bienvenu Gael Fouda-Mbanga, Eswaran Prabakaran, and Kriveshini Pillay†

Department of Chemical Sciences, University of Johannesburg, Doornfontein Campus, Johannesburg 2028, South Africa
(*Received 15 January 2022 • Revised 29 April 2022 • Accepted 23 May 2022*)

TGA Analysis

TGA and DTA were evaluated to establish the thermal stability and decomposition temperature of CNS and CNS/ZrO_2NPs nanocomposite under N_2 atmosphere at temperature ranges from 10-1,000 °C, 10 °C/min as shown in Fig. S1(a) & (b). The TGA and DTG curves of CNS are exhibited as shown in Fig. S1(a). The TGA of CNS revealed that weight loss (13.8%) began at the temperature range of 84 to 238 °C owing to water molecules removal related to CNS surface and a progressive loss of oxygen transporting moieties [1]. The weight loss of 33.22% observed at 238 to 315 °C as shown in Fig. S1(a) was caused by the decomposition of organic functional groups [2]. Another weight loss of 27.96% was observed at 315 to 610 °C which further corresponded to the decomposition or volatilization of organic functional groups. No further decomposition has taken place afterwards. The DTA curve of CNS indicated an exothermic reaction at 349 °C. The TGA of CNS/ZrO_2NPs nanocomposite exhibited a weight loss of 0.25% from 80 to 210 °C which is associated with the removal of water and other impurities. At high temperatures between 210 to 496 °C a weight loss of 2.18%, occurred as displayed in Fig. S1(b). This is associated with the decomposition of CNS on ZrO_2 [3-5]. At higher temperatures of 496 to 594 °C (0.21%), combustion of CNS in CNS/ZrO_2NPs nanocomposite was more favoured. Furthermore, at higher temperature than 600 °C, no weight loss occurred due to the better stability of CNS/ZrO_2NPs nanocomposite than CNS. The DTA curve of CNS/ZrO_2NPs nanocomposite indicates that the reaction was exothermic as shown in Fig. S1(b).

BET Analysis

To ascertain the porosity, pore size and surface area of synthesized CNS and CNS/ZrO_2NPs nanocomposite, nitrogen adsorption-desorption was employed as displayed in Fig. S2(a)-(d). Fig. S2(a) & (b) demonstrated a hysteresis loop with type IV model indicating the mesoporous nature of CNS and CNS/ZrO_2NPs nanocomposite. The surface area of CNS and CNS/ZrO_2NPs nanocomposite was determined as 9.43 and 27.59 m^2g^{-1} as shown in Fig. S2(a) & (b). The increase in surface area in CNS/ZrO_2NPs nanocomposite is due to more available sites which is good for metal adsorption [6]. The Barrett-Joyner-Halenda (BJH) plot was utilized to determine the pore size of CNS (231.62 nm) and CNS/ZrO_2NPs nanocomposite (19.20 nm) as shown in Fig. S2(c) & (d). The distribution of the pore size confirms the presence of micropores and mesopores of CNS and CNS/ZrO_2NPs nanocomposite [7]. The hysteresis loop in this curve is derived from the wedge-shaped capillaries with closed edges at the narrow side [8]. Furthermore, the rapid rise in uptake at relative moderate pressure p/p_o, and wide knee followed by an extended plateau as the pressure increases substantiate the existence of the mesopores and macropores as seen in Fig. S2(c) & (d).

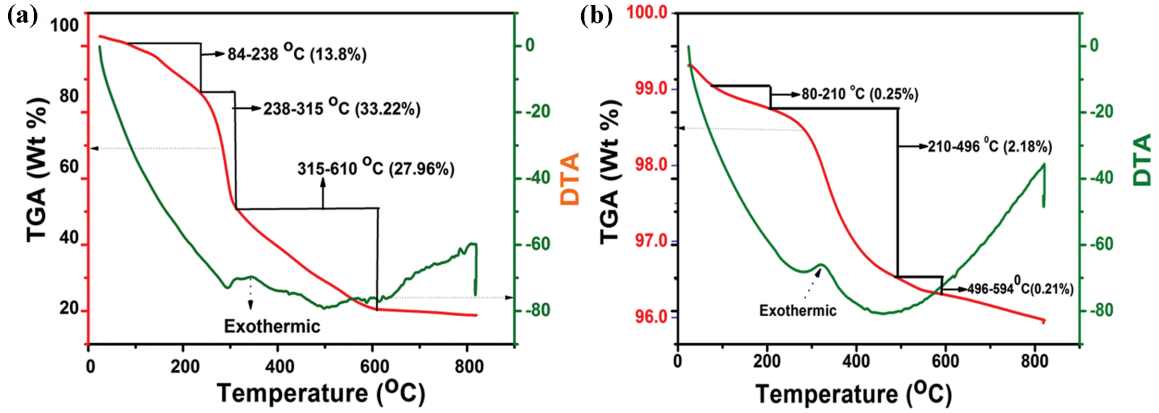


Fig. S1. (a) TGA and DTG spectra of CNS and (b) CNS/ZrO_2NPs nanocomposite.

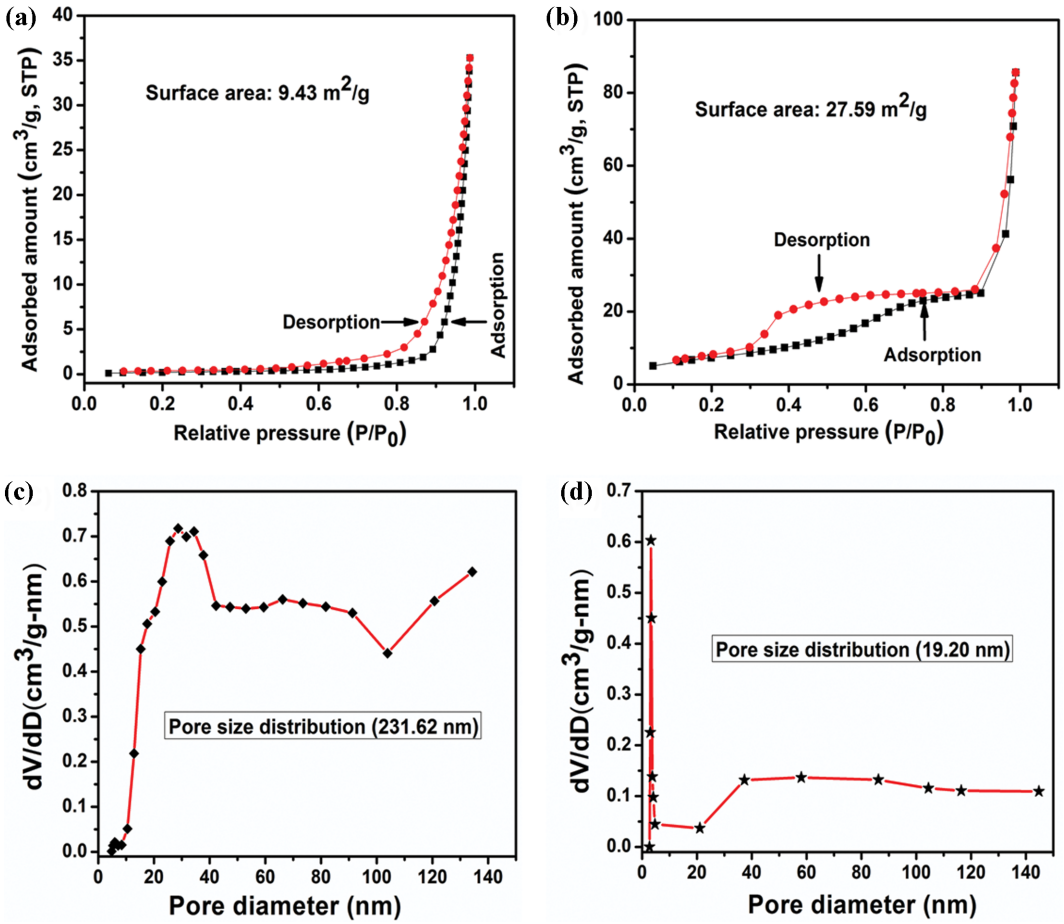


Fig. S2. N_2 adsorption-desorption of processes of (a) CNSs and (b) CNS/ZrO_2NPs nanocomposite and Pore size of (c) CNS and (d) CNS/ZrO_2NPs nanocomposite.

Surface Morphology Analysis

SEM was applied to examine the morphology and crystalline nature of CNS nanocomposite. Fig. S3(A)-(C) displays CNS images acquired at various magnification of 100 μm, 20 μm and 10 μm. At lower magnification of 100 μm, stack granular shaped-l particles were noticed as shown in Fig. S3(A). A clear and well defined carbon nanosheet morphology was observed at higher magnifications of 20 and 10 μm as demonstrated in Fig. S3(B) & (C). Furthermore, the EDX spectrum of CNS exhibited peaks of C and O where carbon was highly abundant as shown in Fig. S3(D).

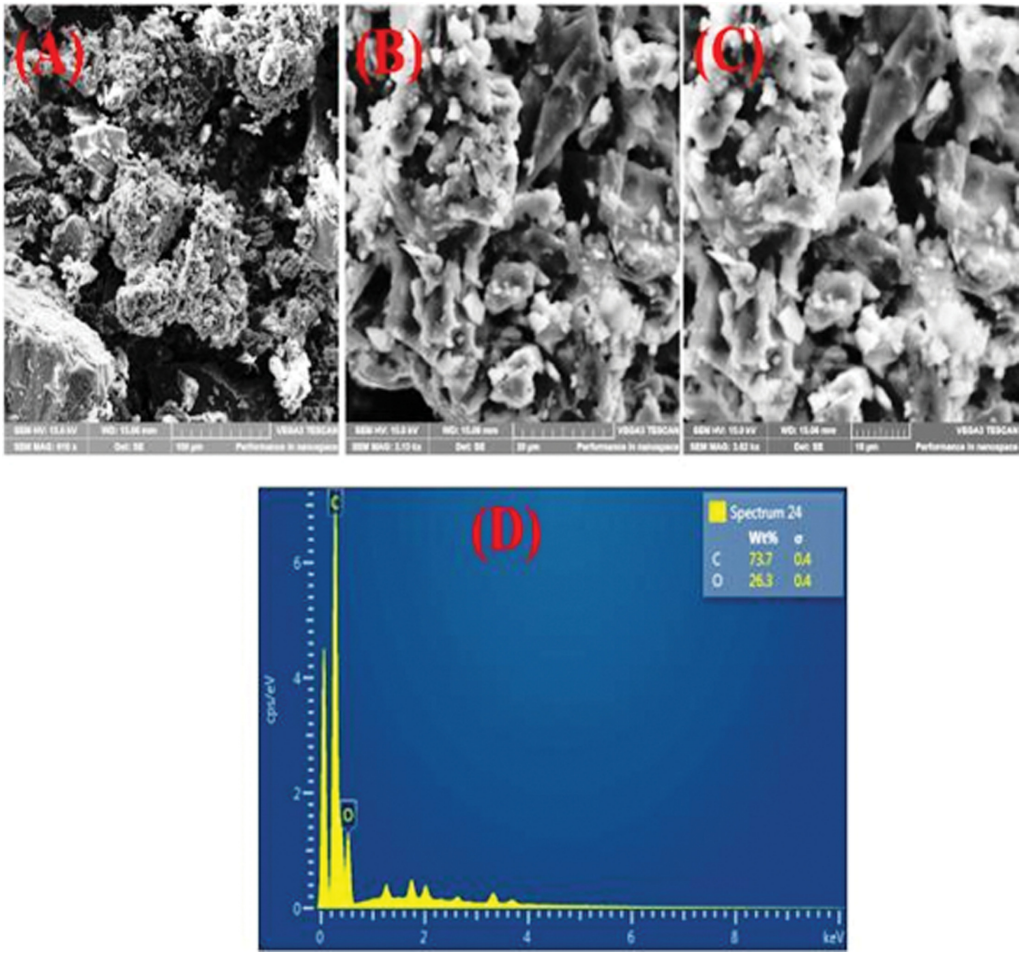


Fig. S3. SEM images of CNS at different magnifications of (A) 100 μm, (B) 20 μm, (C) 10 μm and (D) EDAX.

TEM Characterization

TEM characterization was implemented to figure out the size and shape of CNS with equivalent images perceived at 200, 100 and 50 nm magnification as presented in Fig. S4. The low magnification at 200 and 100 nm displayed a close-packed with spherical shaped structures as seen in Fig. S4(A) & (B). The high magnification at 50 nm demonstrated the porous morphology of carbon nanosheets with strong architectural connection which eventually demonstrated the presence of a high number of mesopores as shown in Fig. S4(C) [9]. Fig. S4(D) shows the particle size distribution of CNS where the size distribution found was 89.13 nm.

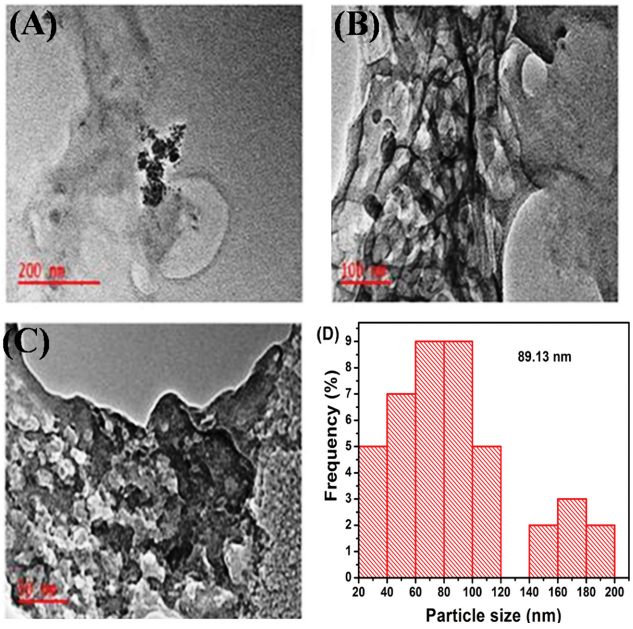


Fig. S4. TEM images of CNS at different magnifications of (A) 200 nm, (B) 100 nm, (C) 50 nm and (D) Histogram of particle size distribution.

Non-linear Isotherm Model

Langmuir Non-linear Model

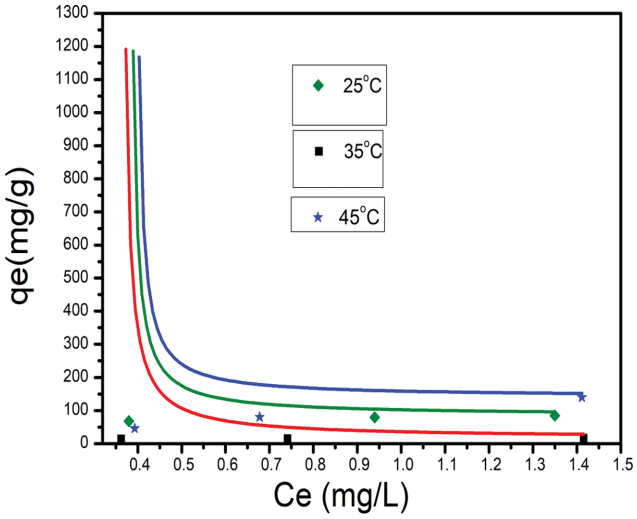


Fig. S5. Langmuir non-linear model of Zn^{2+} ions at 60 min, 200 rpm at different temperature.

Freundlich Non-linear Model

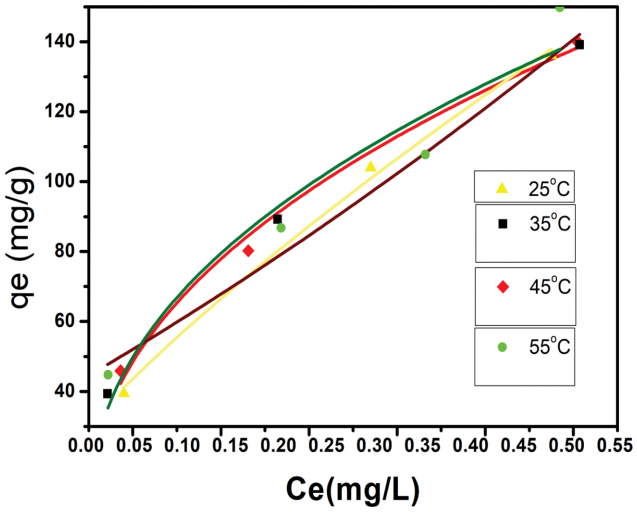


Fig. S6. Freundlich nonlinear model of Zn^{2+} ions at 60 min, 200 rpm at different temperature.

Temkin Non-linear Model

Table S1. Non-linear adsorption isotherm parameter for adsorption of Zn^{2+} ions by CNS/ZrO_2NPs nanocomposite

Parameters	Langmuir	Freundlich	Temkin
q_m (mgg^{-1})	173.34		
K_F		226.23	
K	−1.63		
n		0.87	
K_T			−82.10
B			−0.12
E			
R^2	−0.25	0.95	0.63

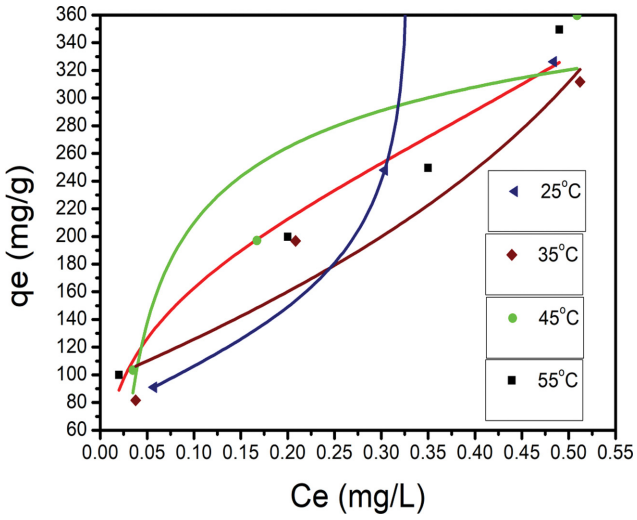


Fig. S7. Temkin non-linear model of Zn^{2+} ions at 60 min, 200 rpm at different temperature.

Fingerprint Ridge Distinctiveness Using Zn^{2+}-CNS/ZrO_2NPs Nanocomposite

Precision in the characterization of fingerprints is very crucial in forensic investigations for lawbreaker's recognition. Fingerprint ridge details were examined to confirm the fingerprint impression and support crime scene investigations [10]. Fig. S8 depicts the fingerprint ridge details that were evaluated using Zn^{2+}-CNS/ZrO_2NPs nanocomposite with aluminium sheet for two donors under day-

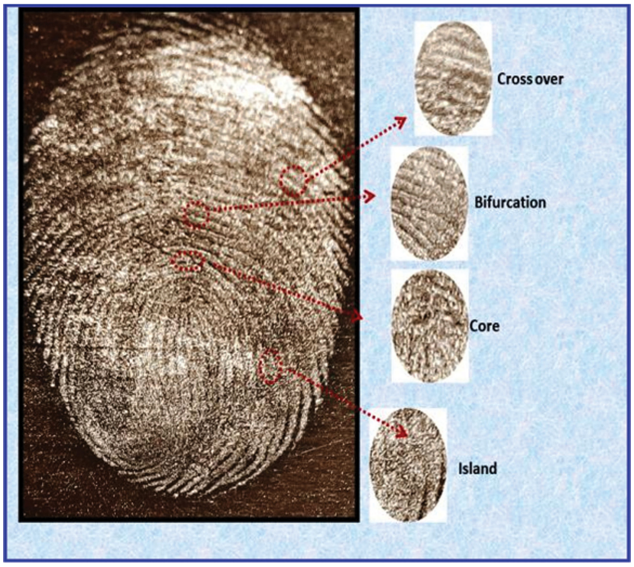


Fig. S8. LFP image with ridge patterns characteristics on aluminum sheet with Zn^{2+}-CNS/ZrO_2NPs nanocomposite by donor 1 under visible light condition.

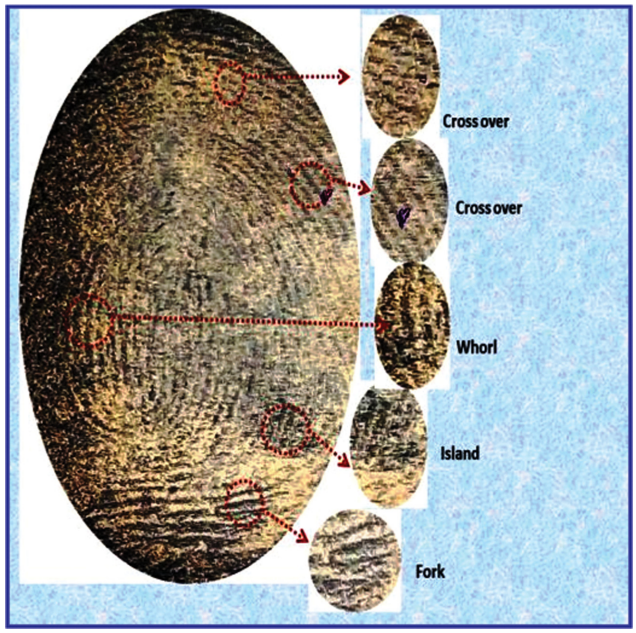
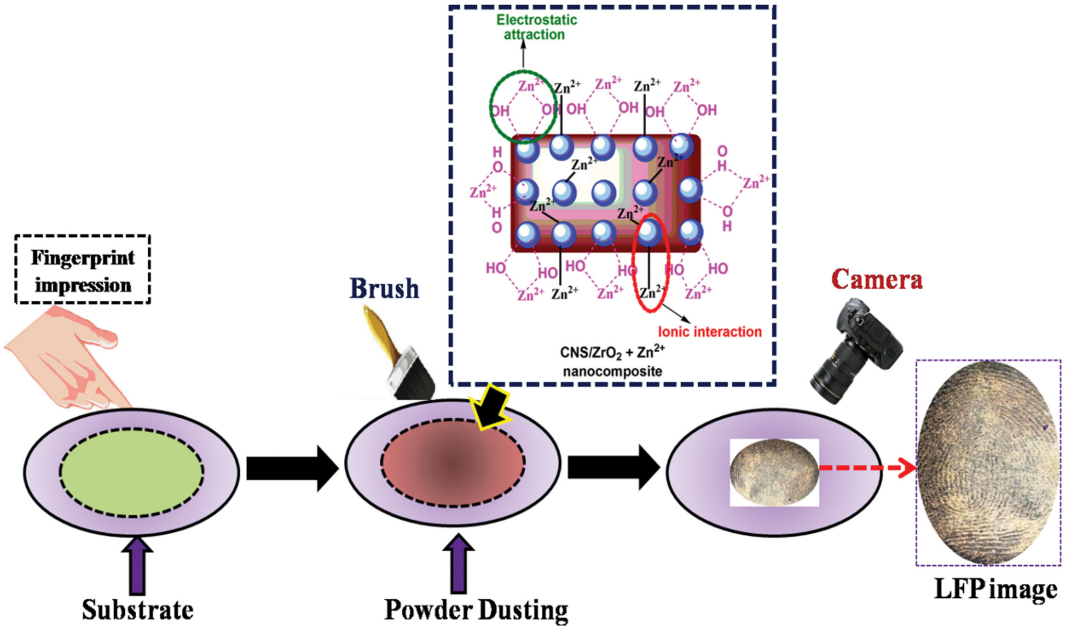


Fig. S9. LFP image with ridge patterns characteristics on aluminum sheet with Zn^{2+}-CNS/ZrO_2NPs nanocomposite by donor 2 under visible light condition.

light conditions. The principal LFP image was represented as level 1 image; level 2 described the ridge pattern of cross-over, bifurcation, core and island for donor 1 as shown in Fig. S8. Donor 2 described and exhibited cross-over, whorl, island, and fork as demonstrated in Fig. S9. These ridge details can be utilized for the identification of an offender. The fingerprint characterizations demonstrated that Zn^{2+}-CNS/ZrO_2NPs nanocomposite powder may be applied as an efficient labeling agent.

Scheme S1 represents the LFP mechanism steps, where the donors' fingers were washed prior to any more work. LFP detection was implemented by applying the powder dusting approach with Zn^{2+}-CNS/ZrO_2NPs nanocomposite as fingerprint powder. Residues of fingerprint contain oil components of amino acids, proteins and peptides. Zn^{2+}-CNS/ZrO_2NPs nanocomposite powder was developed on the fingerprint residue and it strongly coordinated with oil components to yield complex and it gave clear fingerprint image and ridges due to electrostatic interaction between the Zn^{2+}-CNS/ZrO_2NPs nanocomposite and oil components of the fingerprint



Scheme S1. LFP detection mechanisms with Zn^{2+}-CNS/ZrO_2NPs nanocomposite by using powder dusting method.

residue. The extra Zn^{2+}-CNS/ZrO_2NPs nanocomposite powder was removed with a squirrel brush to obtain clear fingerprint images under visible light and latent fingerprint images were taken with a smart phone.

REFERENCES

1. S. Pandey, A. Mewada, M. Thakur, A. Tank and M. Sharon, *RSC Adv.*, **3**, 26290 (2013).
2. V. N. Mehta, S. Jha, R. K. Singhal and S. K. Kailasa, *New J. Chem.*, **38**, 6152 (2014).
3. P. Madkikar, X. Wang, T. Mittermeier, A. H. A. Monteverde Videla, C. Denk, S. Specchia, H. A. Gasteiger and M. Piana, *J. Nanostructure Chem.*, **7**, 133 (2017).
4. A. Bouibed and R. Doufnoune, *J. Adhes. Sci. Technol.*, **33**, 8 (2019).
5. A. O. Romero, C. Montes De Correa and F. Bustamante, *Rev. Fac. Ing. Univ. Antioquia*, **57** (2011).
6. R. S. Das, S. K. Warkhade, A. Kumar and A. V. Wankhade, *Res. Chem. Intermed.*, **45**, 1689 (2019).
7. H. Ait Ahsaine, Z. Anfar, M. Zbair, M. Ezahri and N. EL Alem, *J. Chem.*, **2018** (2018).
8. E. Nouri, M. Shahmiri, H. R. Rezaie and F. Talayian, *Int. J. Ind. Chem.*, **3**, 1 (2012).
9. A. J. S. Ahammad, N. Odhikari, S. S. Shah, M. M. Hasan, T. Islam, P. R. Pal, M. A. Ahmed Qasem and M. A. Aziz, *Nanoscale Adv.*, **1**, 613 (2019).
10. E. Prabakaran and K. Pillay, *Arab. J. Chem.*, **13**, 3817 (2020).